IOP PUBLISHING INVERSE PROBLEMS

Inverse Problems **23** (2007) 2059–2088 doi:10.1088/0266-5611/23/5/015

Grids and transforms for band-limited functions in a disk

Gregory Beylkin, Christopher Kurcz and Lucas Monzón

Department of Applied Mathematics, University of Colorado at Boulder, 526 UCB, Boulder, CO 80309-0526, USA

Received 24 April 2007, in final form 7 August 2007
Published 28 August 2007
Online at stacks.iop.org/IP/23/2059

Abstract

We develop fast discrete Fourier transforms (and their adjoints) from a square in space to a disk in the Fourier domain. Since our new transforms are not unitary, we develop a fast inversion algorithm and derive corresponding estimates that allow us to avoid iterative methods typically used for inversion. We consider the eigenfunctions of the corresponding band-limiting and space-limiting operator to describe spaces on which these new transforms can be inverted and made useful. In the process, we construct polar grids which provide quadratures and interpolation with controlled accuracy for functions band-limited within a disk. For rapid computation of the involved trigonometric sums we use the unequally spaced fast Fourier transform, thus yielding fast algorithms for all new transforms. We also introduce polar grids motivated by linearized scattering problems which are obtained by discretizing a family of circles. These circles are generated by using a single circle passing through the origin and rotating this circle with the origin as a pivot. For such grids, we provide a fast algorithm for interpolation to a near optimal grid in the disk, yielding an accurate adjoint transform and inversion algorithm.

1. Introduction

This paper introduces fast discrete Fourier transforms from a square in the spatial domain to a disk in the Fourier domain. Whereas there are many possible discretizations of the Fourier transform, the new transforms are special in that, under appropriate conditions, we may use the adjoint in lieu of the inverse transform. Unlike the discrete Fourier transform (DFT), these transforms are not unitary and have a numerical null space. For these reasons, we pay special attention to describing spaces on which they may be inverted and made useful. We develop a fast inversion algorithm (and corresponding estimates) that avoids iterative methods typically used for inversion. We note that the speed of all new algorithms is proportional to that of the fast Fourier transform (FFT). In essence, we present an approach for constructing useful analogues of the FFT to and from a polar grid in the Fourier domain.

The need for such fast transforms and associated grids arises in many applications, including problems of non-destructive evaluation such as x-ray tomography, diffraction tomography, synthetic aperture radar and linearized inverse scattering; applications such as image rotation, signal processing, directional bases and many others. In all of these instances, band-limited functions are a natural entity and we expect these fast and accurate new transforms to play a role similar to that of the FFT as a standardized tool for computing Fourier integrals. A new feature of our approach is the design of grids permitting complete accuracy control which should yield improved performance of algorithms for these applications. We provide a few examples of their use in section 6 and indicate a number of applications in section 8.

The key component of our approach is the introduction of special grids for the disk. A crucial property of these grids is that they provide quadratures and interpolation with controlled accuracy for functions band-limited within a disk in the Fourier domain. Unlike the DFT, the transforms of this paper are not exact in algebraic sense but, instead, are constructed for any finite but arbitrary accuracy. Recall that we may arrive at the DFT by using the trapezoidal rule for computing Fourier coefficients; since the trapezoidal rule is exact for trigonometric polynomials (up to an appropriate degree), it yields an algebraically exact discrete transform. With this in mind, we consider the construction of discrete transforms as a problem of developing appropriate quadratures for their Fourier integrals. We present two such grids for the disk, one with minimal (or near minimal) number of nodes for a given bandlimit and accuracy and, another, with quadrature nodes invariant under certain transformations.

In this paper, we consider two cases of spatial discretization of functions on the square: one with equally spaced nodes (appropriate for smooth periodic functions) and the other with quadrature nodes for band-limited functions (which are not necessarily periodic). We construct a nearly optimal grid in the Fourier domain applicable to either spatial discretization. We define the discrete transforms using these grids and analyze spaces of functions (signals) for which the inversion problem yields a numerical solution with controlled accuracy. The approach of this paper relies on the results in [8] describing the construction of generalized Gaussian quadratures for exponentials integrated with the measure $|x|\mathrm{d}x$. We note that example 2 in section 4.3 in [8] has been presented with this application in mind.

We also introduce an alternative Fourier grid motivated by linearized inverse scattering [5, 6, 10, 13]. This remarkable grid is obtained by using equally spaced nodes on a single circle passing through the origin and then rotating it around the origin to generate the entire grid. It is a simple but not an immediately obvious fact that these nodes may also be described as lying on particular concentric circles and diameters of the disk. Although such discretizations have been implicitly used in low order/accuracy computations [13], by themselves they are not well suited for evaluating integrals with controlled accuracy. On the other hand, it is an excellent grid for trigonometric interpolation on rotating circles within the disk. Thus, the inverse DFT from this grid is a two step algorithm, where we first use trigonometric interpolation of the function to a near optimal grid for which we already have an inverse DFT.

Our algorithms rely on the unequally spaced fast Fourier transform (USFFT) [7, 14] and, as a result, all transforms that we perform have the same complexity as the FFT and differ in speed from the FFT only by a factor. This factor depends on the desired accuracy and we refer to [7, 14, 19, 20] for a demonstration of performance of such transforms. Since by now it is a well-established subject matter, we briefly discuss the USFFT in appendix A.

A construction of a polar grid in a square, the pseudo-polar fast Fourier transform (pPFFT) and algorithms for its inversion were presented in [3] (also see references therein). The algorithms in [3] use only one-dimensional FFTs and also provide a non-iterative inversion [4]; however, the pseudo-polar grid does not permit high order interpolation. As a result, such a grid is necessarily oversampled, thus offsetting the benefit of using only one-dimensional

transforms. We did not attempt to compare the speed of the pPFFT and that of our approach. These algorithms have the same order of complexity and their speed may differ only by a factor. Such a factor is difficult to ascertain conclusively, not only due to the details of implementation, but also due to the differences in the required number of grid nodes.

The Fourier transform on an arbitrary grid, including the polar grid, may be evaluated by using the USFFT (a point made in [15]). However, as a consequence of neglecting the quadrature properties of the grid, the inversion of such a transform usually requires solving an ill-conditioned linear system. In [15] and many other papers on applications of the USFFT (see e.g. [2]), the authors use the conjugate gradient method to solve such a system since fast direct solvers are not available. While well justified in many applications, we note that such an approach produces only a nominally fast algorithm since the number of iterations of the conjugate gradient method (controlled by the condition number of the linear system) may be significant. Even if the condition number is reasonable, an iterative approach inflicts a penalty in performance.

We also mention [22] which provides a numerical method for computing Slepian functions for the disk to disk mapping (and the corresponding quadratures), following the analytic construction in [23] and the approach in [27]. The resulting grids are close, but not identical to the nearly optimal grids developed in this paper. It is important to note that the spectrum of the space-limiting and band-limiting operator for the disk to disk mapping in [22, 23] is substantially different from that of this paper which we further explain in remark 5.3.

We start the paper by considering the eigenvalue problem for the space-limiting and band-limiting operator defined for functions concentrated in a square in the spatial domain and in a disk in the Fourier domain. In section 3, we develop near optimal Fourier grids to accurately approximate the kernel of such an operator. Given these grids, we introduce the discrete forward and adjoint transforms in section 4 and consider their inversion in section 5. In section 6, we present several examples of using these transforms. In section 7, we turn our attention to another type of Fourier grids generated by rotating circles. We show how to use the trigonometric interpolation along these rotating circles to compute values of the function on the nearly optimal grids introduced in section 3, thus making it possible to use grids on rotating circles for inversion. We remark on applications and extensions of our results in section 8.

2. Preliminary considerations

In this section, we provide the necessary background by adapting Slepian's original construction [17, 18, 23–26] for our case and introducing appropriate notation.

2.1. Functions band-limited on a disk

It is well known that a function with compactly supported Fourier transform cannot have compact support itself unless it is identically zero. However, this constraint is easily overcome for a finite accuracy. For example, consider a Gaussian and set a threshold on it and its Fourier transform, thus limiting both supports for any finite accuracy. All measurements, being approximate, violate this localization constraint since we never deal with either infinite bandwidth or with functions that extend indefinitely in space or time. Thus, it is natural to analyze the operator whose effect on a function is to truncate it both in spatial and in Fourier domains. This has been the topic of a series of seminal papers by Slepian *et al* [17, 18, 23–26], where it is observed (*inter alia*) that the eigenfunctions of such an operator on a finite interval are the prolate spheroidal wavefunctions (PSWFs) of classical mathematical physics.

In this section, we construct such a Slepian operator by band-limiting functions to a disk and space-limiting them to a square. The choice of a disk and a square is suggested by typical applications. A disk in the Fourier domain is a natural choice for isotropic treatment of directions. Choosing a square in space is relevant in many contexts as well. It turns out, however, that these choices also lead to useful spectral properties of the corresponding Slepian operator, not obtainable in the original construction in [23] (see also [22]).

For a band-limited function f with Fourier transform $\hat{f}$ supported in the disk

$$D_{2c} = \left\{ (p_1, p_2) : \sqrt{p_1^2 + p_2^2} \leqslant 2c \right\},$$

we have

$$f(\mathbf{x}) = f(x_1, x_2) = \frac{1}{(2\pi)^2} \int_{D_{2c}} \hat{f}(p_1, p_2)\, \mathrm{e}^{\mathrm{i}(p_1 x_1 + p_2 x_2)}\, \mathrm{d}p_1\, \mathrm{d}p_2. \tag{1}$$

We choose the disk of radius $2c$ since, in what follows, we will consider the square $B = \left[-\frac{1}{2}, \frac{1}{2}\right] \times \left[-\frac{1}{2}, \frac{1}{2}\right]$ instead of the 'traditional' square $[-1, 1] \times [-1, 1]$. With this choice, the function f in (1) has bandlimit parameter $2c$ and, thus, bandwidth $W = c/\pi$. The bandwidth W appears in discrete transforms and is used in the engineering literature.

We denote by $L^2(B)$ and $L^2(D_{2c})$ the spaces of square integrable functions with the inner products

$$\langle f, g \rangle_B = \int_B f(\mathbf{x}) \bar{g}(\mathbf{x})\, \mathrm{d}\mathbf{x} \tag{2}$$

and

$$\langle \hat{f}, \hat{g} \rangle_{D_{2c}} = \frac{1}{4\pi^2} \int_{D_{2c}} \hat{f}(\mathbf{p}) \bar{\hat{g}}(\mathbf{p})\, \mathrm{d}\mathbf{p}. \tag{3}$$

In order to identify a useful class of functions, we consider a function f supported in B with Fourier transform

$$\hat{f}(\mathbf{p}) = \mathcal{F}_{2c}[f](\mathbf{p}) = \int_B f(\mathbf{x})\, \mathrm{e}^{-\mathrm{i}\mathbf{x}\cdot\mathbf{p}}\, \mathrm{d}\mathbf{x}, \tag{4}$$

and restrict the support of $\hat{f}$ to the disk of radius $2c$, so that

$$\mathcal{F}_{2c} : L^2(B) \to L^2(D_{2c}).$$

We then consider the adjoint transform

$$\mathcal{F}_{2c}^*[\hat{g}](\mathbf{x}) = \frac{1}{4\pi^2} \int_{D_{2c}} \hat{g}(\mathbf{p})\, \mathrm{e}^{\mathrm{i}\mathbf{x}\cdot\mathbf{p}}\, \mathrm{d}\mathbf{p}, \tag{5}$$

and limit the support of the resulting function to the square B, so that

$$\mathcal{F}_{2c}^* : L^2(D_{2c}) \to L^2(B).$$

We now define the band-limiting and space-limiting operator as

$$\mathcal{Q}_{2c} = \mathcal{F}_{2c}^* \mathcal{F}_{2c} : L^2(B) \to L^2(B),$$

where

$$\mathcal{Q}_{2c}[f](\mathbf{x}) = \frac{1}{4\pi^2} \int_{D_{2c}} \hat{f}(\mathbf{p})\, \mathrm{e}^{\mathrm{i}\mathbf{x}\cdot\mathbf{p}}\, \mathrm{d}\mathbf{p}.$$

The compact positive definite operator $\mathcal{Q}_{2c}$ acts as a convolution with kernel

$$K_{2c}(\mathbf{x}) = K_{2c}(x_1, x_2) = \frac{1}{4\pi^2} \int_{D_{2c}} \mathrm{e}^{\mathrm{i}\mathbf{p}\cdot\mathbf{x}}\, \mathrm{d}\mathbf{p} = \frac{c J_1\left(2c\sqrt{x_1^2 + x_2^2}\right)}{\pi\sqrt{x_1^2 + x_2^2}}, \tag{6}$$

where $\mathbf{x} \in 2B$. Following [23–26], we are interested in finding the eigenvalues and the eigenfunctions of $\mathcal{Q}_{2c}$. We consider the eigenvalue problem

$$\mu_j \psi_{j,2c}(\mathbf{y}) = \int_B K_{2c}(\mathbf{y}-\mathbf{z})\psi_{j,2c}(\mathbf{z})\,\mathrm{d}\mathbf{z}, \tag{7}$$

where $\mathbf{y}, \mathbf{z} \in B$, $j = 0, 1, 2, \ldots$ and $1 > \mu_0 > \mu_1 \geqslant \mu_2 \geqslant \cdots$. We briefly discuss the spectral properties of the operator $\mathcal{Q}_{2c}$ in appendix A.1. For brevity of notation, we drop the dependence of the eigenfunctions on c and write $\psi_{j,2c} = \psi_j$. The eigenfunctions of $\mathcal{Q}_{2c}$ are real valued, and we normalize them so that

$$\|\psi_j\|_B = \left(\int_B |\psi_j(\mathbf{z})|^2\,\mathrm{d}\mathbf{z}\right)^{1/2} = 1. \tag{8}$$

The operator $\mathcal{Q}_{2c}$ plays a key role in the construction of Fourier grids (see section 3).

Next we consider two discrete versions of the eigenproblem (7), derived by equally or unequally spaced discretization of the spatial domain. The former discretization is intended for band-limited functions periodic in B and the latter for band-limited but not necessarily periodic functions.

2.2. Equally spaced discretization in the spatial domain

Let us consider a case where we are given a finite set of values of a function f in (1):

$$f_{mn} = f\left(-\frac{1}{2}+\frac{m}{N}, -\frac{1}{2}+\frac{n}{N}\right), \tag{9}$$

evaluated on the equally spaced grid in B denoted as

$$\mathbf{x}^e = \left\{\mathbf{x}^e_{mn}\right\}_{m,n=0}^{N-1} = \left\{\left(-\frac{1}{2}+\frac{m}{N}, -\frac{1}{2}+\frac{n}{N}\right)\right\}_{m,n=0}^{N-1}. \tag{10}$$

In this case, we may refer to $\mathbf{f}_e = \{f_{mn}\}_{m,n=0}^{N-1}$ as a discrete signal or simply a signal to distinguish this common occurrence from problems where we control the manner of discretization of f on B. For these signals, we use the (usual) inner product obtained by uniform discretization of (2):

$$\langle \mathbf{f}_e, \mathbf{g}_e\rangle = \frac{1}{N^2}\sum_{m,n=0}^{N-1} f_{mn}\bar{g}_{mn}. \tag{11}$$

We now define analogues of transforms (4) and (5) for the critically sampled case where

$$c = \frac{\pi N}{2}. \tag{12}$$

Let $D = D_1 = \left\{(p_1, p_2) : \sqrt{p_1^2 + p_2^2} \leqslant 1\right\}$ be the unit disk in the Fourier domain. We define the forward transform as

$$F_e : \mathbb{C}^{N^2} \to L^2_D$$

$$\hat{f}_e(\mathbf{p}) = F_e[\mathbf{f}_e](\mathbf{p}) = \frac{1}{N^2}\sum_{m,n=0}^{N-1} f_{mn}\,\mathrm{e}^{-\mathrm{i}\pi N\mathbf{p}\cdot\mathbf{x}^e_{mn}}, \tag{13}$$

where $\mathbb{C}^{N^2}$ is considered with the inner product (11). Here L^2_D is the space of square integrable functions in the unit disk with the inner product induced by (3), our choice of c in (12) and a simple rescaling to the unit disk. Thus, the adjoint transform is given by

$$F_e^* : L^2_D \to \mathbb{C}^{N^2},$$

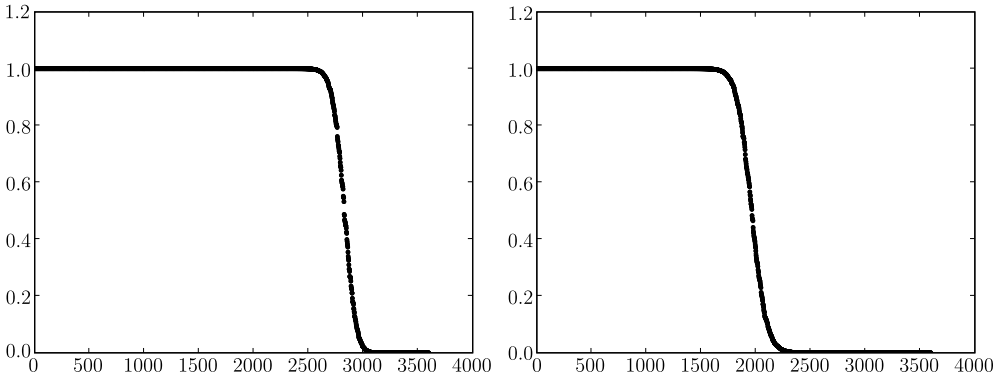

Figure 1. Eigenvalues of (16) and (25) for equally and unequally spaced discretization in space with $N = N_\omega = 60$.

$$F_e^*[\hat{g}]_{mn} = \frac{N^2}{4} \int_D \hat{g}(\mathbf{p})\, \mathrm{e}^{\mathrm{i}\pi N \mathbf{p}\cdot\mathbf{x}^e_{mn}}\, \mathrm{d}\mathbf{p}, \tag{14}$$

where the grid $\mathbf{x}^e_{mn}$ is defined by (10).

Next, we consider a composition of the forward and the adjoint transforms, $Q_e = F_e^* F_e$,

$$Q_e : \mathbb{C}^{N^2} \to \mathbb{C}^{N^2},$$

$$Q_e[\mathbf{f}_e]_{mn} = \frac{N^2}{4} \int_D \hat{f}_e(\mathbf{p})\, \mathrm{e}^{\mathrm{i}\pi N \mathbf{p}\cdot\mathbf{x}^e_{mn}}\, \mathrm{d}\mathbf{p}.$$

The matrix elements of Q_e are given by the discretized kernel (6),

$$(Q_e)_{mn,m'n'} = \frac{1}{N^2} K_{\pi N}\left(\frac{m-m'}{N}, \frac{n-n'}{N}\right). \tag{15}$$

We compute the eigenvalues and eigenvectors of the symmetric eigenproblem

$$\begin{aligned}\mu^e_j \psi^e_{j,mn} &= \sum_{m',n'=0}^{N-1} (Q_e)_{mn,m'n'} \psi^e_{j,m'n'} \\ &= \sum_{m',n'=0}^{N-1} \frac{J_1\left(\pi N \sqrt{\left(\frac{m}{N}-\frac{m'}{N}\right)^2 + \left(\frac{n}{N}-\frac{n'}{N}\right)^2}\right)}{2N\sqrt{\left(\frac{m}{N}-\frac{m'}{N}\right)^2 + \left(\frac{n}{N}-\frac{n'}{N}\right)^2}} \psi^e_{j,m'n'},\end{aligned} \tag{16}$$

with

$$\left\langle \psi^e_j, \psi^e_{j'} \right\rangle = \delta_{jj'}. \tag{17}$$

The spectrum of (16) and several eigenvectors are illustrated in figures 1 and 2.

2.3. Unequally spaced discretization in the spatial domain

Let us consider the case where we control how to discretize the functions in (7). In order to accommodate band-limited, non-periodic functions, we select a tensor product grid associated with generalized Gaussian quadratures for band-limited functions (see [8, 27]).

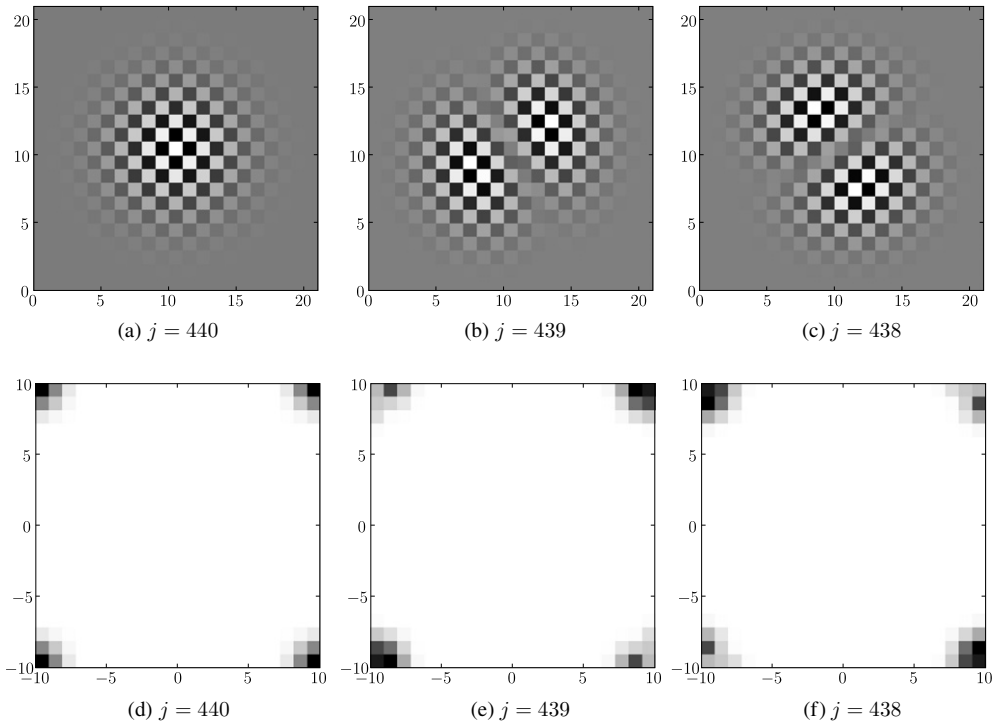

(a) $j = 440$ (b) $j = 439$ (c) $j = 438$

(d) $j = 440$ (e) $j = 439$ (f) $j = 438$

Figure 2. The last three eigenvectors of (16) (top row) and the magnitude of their discrete Fourier transforms (bottom row) for $N = 21$. Significant values in the bottom row are indicated as black. Since these eigenvectors correspond to eigenvalues close to zero, they are effectively in the null space of the operator; their Fourier transforms are supported essentially outside the disk D_{2c}.

Following [8] we compute, for some $\epsilon_\omega > 0$ and bandlimit $2c$, the nodes $|\theta_k| < 1$ and the weights $\omega_k > 0$, $k = 0, \ldots, N_\omega - 1$, where $N_\omega = N_\omega(c, \epsilon_\omega)$, such that for all $y \in [-1, 1]$

$$\left| \int_{-1}^{1} \mathrm{e}^{\mathrm{i}2c\theta y} \, \mathrm{d}\theta - \sum_{k=0}^{N_\omega - 1} \omega_k \, \mathrm{e}^{\mathrm{i}2c\theta_k y} \right| \leqslant \epsilon_\omega. \tag{18}$$

We note that selecting the spatial discretization via (18) is nearly optimal as described in [8]. We form the tensor product grid in B

$$\mathbf{x}^\omega = \left\{ \mathbf{x}^\omega_{mn} \right\}_{m,n=0}^{N_\omega - 1} = \left\{ \left(\frac{\theta_m}{2}, \frac{\theta_n}{2} \right) \right\}_{m,n=0}^{N_\omega - 1} \tag{19}$$

and assign the associated weights,

$$\omega_{mn} = \frac{\omega_m \omega_n}{4}. \tag{20}$$

The factors of 2 and 4 in (19) and (20) account for the size of the square B relative to the standard square for quadratures $[-1, 1] \times [-1, 1]$. Using these nodes and weights, we discretize (2) to obtain the inner product

$$\langle \mathbf{f}_\omega, \mathbf{g}_\omega \rangle_\omega = \sum_{m,n=0}^{N_\omega - 1} \omega_{mn} \, f\left(\mathbf{x}^\omega_{mn}\right) \bar{g}\left(\mathbf{x}^\omega_{mn}\right), \tag{21}$$

where vectors $\mathbf{f}_\omega$ and $\mathbf{g}_\omega$ are function values on the grid $\mathbf{x}^\omega$. We now define analogues of (4) and (5) for this unequally spaced case:

$$\begin{aligned} &F_{\omega,2c} : \mathbb{C}_\omega^{N_\omega^2} \to L^2_{D,2c}, \\ &\hat{f}_\omega(\mathbf{p}) = F_{\omega,2c}[\mathbf{f}_\omega](\mathbf{p}) = \sum_{m,n=0}^{N_\omega-1} \omega_{mn} f\left(\mathbf{x}^\omega_{mn}\right) \mathrm{e}^{-\mathrm{i}2c\mathbf{p}\cdot\mathbf{x}^\omega_{mn}}, \end{aligned} \tag{22}$$

where $\mathbb{C}_\omega^{N_\omega^2}$ is considered with the inner product (21). Here, $L^2_{D,2c}$ is the space of square integrable functions in the unit disk with the inner product induced by (3) rescaled to the unit disk.

The adjoint transform is given by

$$F^*_{\omega,2c} : L^2_{D,2c} \to \mathbb{C}_\omega^{N_\omega^2}, \qquad F^*_{\omega,2c}[\hat{g}]_{mn} = \frac{c^2}{\pi^2} \int_D \hat{g}(\mathbf{p}) \, \mathrm{e}^{\mathrm{i}2c\mathbf{p}\cdot\mathbf{x}^\omega_{mn}} \, \mathrm{d}\mathbf{p}, \tag{23}$$

where the grid $\mathbf{x}^\omega_{mn}$ and the weights ω^ω_{mn} are given by (19) and (20) respectively. We then consider $Q_{\omega,2c} = F^*_{\omega,2c} F_{\omega,2c}$,

$$Q_{\omega,2c} : \mathbb{C}_\omega^{N_\omega^2} \to \mathbb{C}_\omega^{N_\omega^2}, \qquad Q_{\omega,2c}[\mathbf{f}_\omega]_{mn} = \frac{c^2}{\pi^2} \int_D \hat{f}_\omega(\mathbf{p}) \, \mathrm{e}^{\mathrm{i}2c\mathbf{p}\cdot\mathbf{x}^\omega_{mn}} \, \mathrm{d}\mathbf{p},$$

where

$$\left(Q_{\omega,2c}\right)_{mn,m'n'} = K_{2c}\left(\frac{\theta_m - \theta_{m'}}{2}, \frac{\theta_n - \theta_{n'}}{2}\right) \omega_{m'n'}. \tag{24}$$

In order to find the eigenvectors of $Q_{\omega,2c}$, we first consider the symmetric eigenvalue problem

$$\mu^\omega_j q^\omega_{j,mn} = \sum_{m',n'=0}^{N_\omega-1} \sqrt{\omega_{mn}} K_{2c}\left(\frac{\theta_m - \theta_{m'}}{2}, \frac{\theta_n - \theta_{n'}}{2}\right) \sqrt{\omega_{m'n'}} q^\omega_{j,m'n'}, \tag{25}$$

where the real eigenvectors $q^\omega_j = \left\{q^\omega_{j,mn}\right\}_{m,n=0}^{N_\omega-1}$ are orthonormal with respect to the standard inner product. The problem in (25) uses the matrix representation of the operator $Q_{\omega,2c}$ with respect to the inner product (21). We then define vectors

$$\psi^\omega_j = \left\{\frac{1}{\sqrt{\omega_{mn}}} q^\omega_{j,mn}\right\}_{m,n=0}^{N_\omega-1}, \tag{26}$$

which now solve the eigenvalue problem

$$Q_{\omega,2c}\psi^\omega_j = \mu^\omega_j \psi^\omega_j. \tag{27}$$

We normalize the eigenvectors ψ^ω_j with respect to the inner product (21),

$$\left\langle \psi^\omega_j, \psi^\omega_{j'} \right\rangle_\omega = \delta_{jj'}. \tag{28}$$

The spectrum of the problem in (27) is illustrated in figure 1. We note that, for an identical matrix size, there are fewer eigenvalues close to one for problem in (27) than for problem in (16). The difference is a consequence of removing the restriction of function periodicity necessary to justify the equally spaced discretization in the spatial domain. In the limit, as the number of points $N_\omega \to \infty$, the difference between the two spectra in figure 1 disappears.

Further discussion of the approximation of (18) by using quadratures can be found in [8, 27]. Given that the transforms are approximate by construction, we also apply them to functions which are only approximately band-limited within the accuracy of the transform. In what follows, we only study the discrete problems (16) and (27). We assume that ϵ_ω and the

bandlimit c have been selected and serve the purpose of providing an approximation to the original problem (7) with accuracy no worse than ϵ_ω.

We now turn to the discretization of the Fourier representation of the kernel K_{2c} maintaining accuracy at a threshold ϵ. We note that for the problem (27), it is natural to consider $\epsilon \geqslant \epsilon_\omega$.

3. Discretization of the kernel

In this section, we construct Fourier grids that provide accurate quadratures for exponential functions (with an appropriate measure) in the disk D. One of our goals is to define and invert the discrete transforms on the linear span of eigenvectors corresponding to significant eigenvalues in (16) and (27). For this reason, we need a Fourier grid to accurately approximate the kernel of the space-limiting and band-limiting operator $\mathcal{Q}_{2c}$ introduced in the previous section.

Toward this end, we discretize the integral representation (6) of the real-valued kernel K_{2c}. Using polar coordinates in (6) with $p_1 = 2c\rho\cos\theta$, $p_2 = 2c\rho\sin\theta$, and $\mathrm{d}p_1\,\mathrm{d}p_2 = 4c^2\rho\,\mathrm{d}\rho\,\mathrm{d}\theta$, we write the kernel as

$$\begin{aligned} K_{2c}(\mathbf{x}) &= \frac{c^2}{\pi^2}\int_0^{2\pi}\int_0^1 \mathrm{e}^{\mathrm{i}2c\rho(x_1\cos\theta+x_2\sin\theta)}\rho\,\mathrm{d}\rho\,\mathrm{d}\theta \\ &= \frac{c^2}{2\pi^2}\int_0^{2\pi}\left(\int_{-1}^1 \mathrm{e}^{\mathrm{i}2c\rho(x_1\cos\theta+x_2\sin\theta)}|\rho|\mathrm{d}\rho\right)\mathrm{d}\theta. \end{aligned} \tag{29}$$

Since $\mathbf{x}\in 2B$, it follows that $|x_1\cos\theta + x_2\sin\theta| \leqslant \sqrt{2}$. Next, we discretize the radial integral in (29) using the generalized Gaussian quadratures for integrating exponential functions with measure $|\rho|\mathrm{d}\rho$. Following [8], we compute for given $\epsilon > 0$ and bandlimit $2\sqrt{2}c > 0$ the nodes $|\rho_k| < 1$ and the weights $w_k > 0$, $k = 1,\ldots,M$, where $M = M(c,\epsilon)$, such that for all $y\in[-1,1]$

$$\left|\int_{-1}^1 \mathrm{e}^{\mathrm{i}2\sqrt{2}c\rho y}|\rho|\mathrm{d}\rho - \sum_{k=1}^M w_k\,\mathrm{e}^{\mathrm{i}2\sqrt{2}c\rho_k y}\right| \leqslant \frac{\pi\epsilon}{c^2}. \tag{30}$$

Results in [8] indicate that the number of terms is proportional to

$$M \sim c + A_1\log c + A_2\log\epsilon^{-1}, \tag{31}$$

where A_1 and A_2 are small constants as is the case for integration with the measure $\mathrm{d}\rho$ leading to the nodes for PSWFs.

Due to the symmetry of the measure, the nodes in (30) are symmetric with respect to the origin so that $\rho_{M-k+1} = -\rho_k$ and $w_{M-k+1} = w_k$ (see example 2 in section 4.3 in [8]). An example of the quadrature nodes and weights is shown in figure 3.

Using (29) and (30), we obtain for $\mathbf{x}\in 2B$,

$$\left|K_{2c}(\mathbf{x}) - \frac{c^2}{2\pi^2}\int_0^{2\pi}\left(\sum_{k=1}^M w_k\,\mathrm{e}^{\mathrm{i}2c\rho_k(x_1\cos\theta+x_2\sin\theta)}\right)\mathrm{d}\theta\right| \leqslant \epsilon. \tag{32}$$

Discretization of (32) in the angle θ proceeds via one of the next two (consistent) approaches.

3.1. Uniform angular discretization

We use the trapezoidal rule and select the number of nodes, L, so that the discretization is accurate for all radii ρ_k, $k = 1,\ldots,M$. The angular integral is then approximated by

$$\left|\frac{c^2}{2\pi^2}\int_0^{2\pi}\mathrm{e}^{\mathrm{i}2c\rho_k(x_1\cos\theta+x_2\sin\theta)}\,\mathrm{d}\theta - \frac{c^2}{L\pi}\sum_{l=0}^{L-1}\mathrm{e}^{\mathrm{i}2c\rho_k(x_1\cos\theta_l+x_2\sin\theta_l)}\right| \leqslant \epsilon, \tag{33}$$

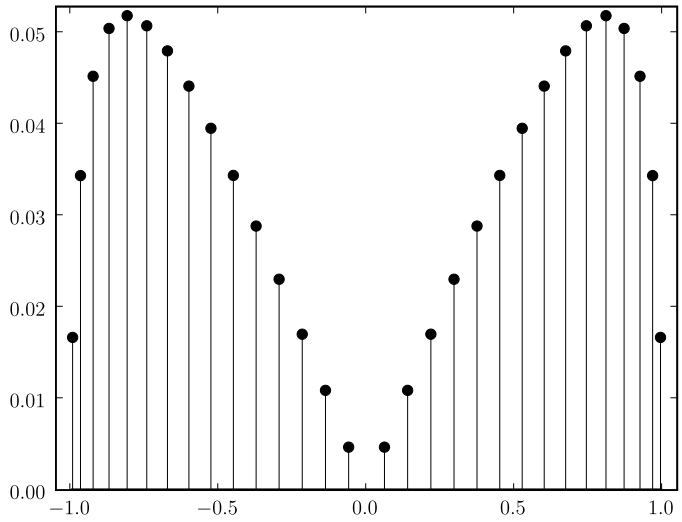

Figure 3. Weights as a function of their radial nodes in (30) for $M = 30$, $\epsilon \approx 9.75 \times 10^{-6}$ and $c \approx 23.324$. As expected, the weights mimic the measure $|\rho| \mathrm{d}\rho$.

where $\theta_l = 2\pi l/L$. In this case, it is sufficient to use L for the largest ρ_k (see below how to select L). We obtain

$$\left| K_{2c}(\mathbf{x}) - \frac{c^2}{L\pi} \sum_{l=0}^{L-1} \sum_{k=1}^{M} w_k \, \mathrm{e}^{\mathrm{i}2c\rho_k(x_1 \cos\theta_l + x_2 \sin\theta_l)} \right| \leqslant 2\epsilon. \tag{34}$$

Although the number of nodes in (34) is excessive on circles close to the origin in the Fourier domain, in many applications it may be convenient to locate nodes on the disk diameters.

We note that (34) has roughly twice as many terms (depending on the parity of M) than needed since (29) introduces a double coverage of the disk. When computing with this formula, we use only the nodes with $\rho_k \geqslant 0$ and $\theta_l \in [0, 2\pi]$.

3.2. Optimized angular discretization

We use the trapezoidal rule and select the number of nodes, L_k, so that the discretization is accurate for each radius ρ_k, $k = 1, \ldots, M$,

$$\left| \frac{c^2}{2\pi^2} \int_0^{2\pi} \mathrm{e}^{\mathrm{i}2c\rho_k(x_1 \cos\theta + x_2 \sin\theta)} \, \mathrm{d}\theta - \frac{c^2}{L_k\pi} \sum_{l=0}^{L_k-1} \mathrm{e}^{\mathrm{i}2c\rho_k(x_1 \cos\theta_{kl} + x_2 \sin\theta_{kl})} \right| \leqslant \epsilon, \tag{35}$$

where $\theta_{kl} = \frac{2\pi l}{L_k}$. This has the effect of reducing the number of nodes as the radius ρ_k becomes smaller. As a result, we obtain

$$\left| K_{2c}(\mathbf{x}) - \sum_{k=1}^{M} \frac{c^2 w_k}{L_k\pi} \sum_{l=0}^{L_k-1} \mathrm{e}^{\mathrm{i}2c\rho_k(x_1 \cos\theta_{kl} + x_2 \sin\theta_{kl})} \right| \leqslant 2\epsilon. \tag{36}$$

To find an appropriate number of nodes L or L_k to be used for the trapezoidal rule in (33) or (35), we replace in (32) $x_1 = \|\mathbf{x}\| \cos\phi$ and $x_2 = \|\mathbf{x}\| \sin\phi$, where $\|\mathbf{x}\| = \sqrt{x_1^2 + x_2^2}$, to obtain

$$\frac{c^2}{2\pi^2} \int_0^{2\pi} \mathrm{e}^{\mathrm{i}2c\rho_k\|\mathbf{x}\| \cos(\theta-\phi)} \, \mathrm{d}\theta = \frac{c^2}{\pi} J_0(2c\rho_k\|\mathbf{x}\|), \tag{37}$$

and thus (32) is equivalent to

$$\left| K_{2c}(\mathbf{x}) - \frac{c^2}{\pi} \sum_{k=1}^{M} w_k J_0(2c\rho_k \|\mathbf{x}\|) \right| \leqslant \epsilon. \tag{38}$$

Our goal is to approximate, for accuracy ϵ, the Bessel function $J_0(2c\rho_k\|\mathbf{x}\|)$ by a trigonometric polynomial, separately for each ρ_k. Since $\mathbf{x} \in 2B$, we approximate $J_0(b)$ for $b = 2\sqrt{2}c\rho_k$ using

$$J_0(b) = \frac{1}{2\pi} \int_0^{2\pi} \mathrm{e}^{\mathrm{i}b\cos\varphi}\, \mathrm{d}\varphi = \frac{1}{2\pi} \int_0^{2\pi} \cos(b\cos\varphi)\, \mathrm{d}\varphi. \tag{39}$$

We note that the integrand in (39) has the Fourier expansion (see e.g. [1, 9.1.44])

$$\cos(b\cos\varphi) = J_0(b) + 2\sum_{j=1}^{\infty} (-1)^j J_{2j}(b) \cos 2j\varphi, \tag{40}$$

where the coefficients decay exponentially fast. In fact, using [1, 9.1.62] with $b > 0$, we have

$$|J_{2j}(b)| \leqslant \frac{b^{2j}}{(2j)!2^{2j}}. \tag{41}$$

Thus, the series in (40) may be truncated to yield a trigonometric polynomial of degree L. Since the trapezoidal rule with appropriately chosen nodes is exact for trigonometric polynomials, we obtain

$$\left| J_0(b) - \frac{1}{L} \sum_{l=0}^{L-1} \cos\left(b\cos\frac{2\pi l}{L} \right) \right| \leqslant \epsilon, \tag{42}$$

as a discretization of (39) (see e.g. [12, Problem 6, section 7.4]). We note that rotating such grids by an angle φ, i.e. $2\pi l/L + \varphi$ in (42), produces an equally valid quadrature, a property we will use later. The number of nodes is chosen as small as possible in (33) or (35). In fact, it is sufficient to choose

$$L_k \geqslant \frac{e}{\sqrt{2}} c\rho_k + \frac{1}{2} \log \epsilon^{-1}. \tag{43}$$

We summarize our discretization of (6) as

Proposition 3.1. *The kernel*

$$K_{2c}(\mathbf{x}) = \frac{1}{4\pi^2} \int_{D_{2c}} \mathrm{e}^{\mathrm{i}\mathbf{x}\cdot\mathbf{p}}\, \mathrm{d}\mathbf{p} \tag{44}$$

may be approximated for any $\epsilon > 0$ via

$$\left| K_{2c}(\mathbf{x}) - \sum_{k,l} \sigma_k \mathrm{e}^{\mathrm{i}2c\mathbf{p}_{kl}\cdot\mathbf{x}} \right| \leqslant \epsilon, \tag{45}$$

where $\mathbf{x} \in 2B = [-1, 1] \times [-1, 1]$, $\mathbf{p}_{kl} = \rho_k (\cos\theta_{kl}, \sin\theta_{kl})$, θ_{kl} are either $\frac{2\pi l}{L}$ or $\frac{2\pi l}{L_k}$, and σ_k denote the weights in either (34) or (36), $\sigma_k = \frac{c^2 w_k}{L\pi}$ or $\sigma_k = \frac{c^2 w_k}{L_k \pi}$. Parameters ρ_k, w_k, L and L_k are described in the previous discussion.

We note that the nodes $\mathbf{p}_{kl}$ and the weights σ_k depend on the bandlimit $2c$.

Remark 3.1. The number of nodes in proposition 3.1 depends only weakly on the accuracy ϵ and may be estimated by the product $M \cdot L$, where M is given in (31) and $L \geqslant \frac{e}{\sqrt{2}} c + \frac{1}{2} \log \epsilon^{-1}$ as it follows from (43).

4. Square to disk discrete Fourier transforms

We now introduce discrete transforms for (13), (14), (22) and (23), where we replace integrals in the Fourier domain by discrete sums using the approximation in proposition 3.1.

Using the Fourier grid and the corresponding weights given in proposition 3.1, we discretize (3) to obtain the inner product

$$\langle f, g\rangle_\sigma = \sum_{kl} \sigma_k f_{kl} \bar{g}_{kl}, \tag{46}$$

where f_{kl}, g_{kl} are values of functions on that grid.

4.1. Equally spaced discretization in the spatial domain

We introduce a fully discrete version of transforms in (13) and (14),

$$\begin{aligned} &G_e : \mathbb{C}^{N^2} \to \mathbb{C}^{N_\sigma^2}, \\ &f_e^\sharp(\mathbf{p}_{kl}) = G_e[\mathbf{f}_e](\mathbf{p}_{kl}) = \frac{1}{N^2} \sum_{m,n=0}^{N-1} f_{mn}\, \mathrm{e}^{-\mathrm{i}\pi N \mathbf{p}_{kl}\cdot\mathbf{x}_{mn}^e} \end{aligned} \tag{47}$$

and

$$\begin{aligned} &G_e^* : \mathbb{C}^{N_\sigma^2} \to \mathbb{C}^{N^2}, \\ &G_e^*[g]_{mn} = \sum_{kl} \sigma_k g_{kl}\, \mathrm{e}^{\mathrm{i}\pi N \mathbf{p}_{kl}\cdot\mathbf{x}_{mn}^e}, \end{aligned} \tag{48}$$

where the nodes $\mathbf{p}_{kl}$ and the weights σ_k are given in proposition 3.1, and the spatial nodes $\mathbf{x}_{mn}^e$ are given by (10). Here N_σ is the total number of nodes $\mathbf{p}_{kl}$ in the Fourier domain, and the total number of nodes $\mathbf{x}_{mn}^e$ in the spatial domain is N^2. Note that

$$(G_e^* G_e)_{mn,m'n'} = \frac{1}{N^2} \sum_{kl} \sigma_k\, \mathrm{e}^{\mathrm{i}\pi N \mathbf{p}_{kl}\cdot(\mathbf{x}_{mn}^e - \mathbf{x}_{m'n'}^e)}. \tag{49}$$

Let us denote the eigenvector of (16) by $\psi_j^e = \{\psi_{mn}^e\}_{m,n=0}^{N-1}$, and define its image in the Fourier domain

$$\psi_j^{\sharp,e}(\mathbf{p}_{kl}) = G_e\big[\psi_j^e\big]. \tag{50}$$

We obtain

$$\big\langle \psi_j^{\sharp,e}, \psi_{j'}^{\sharp,e}\big\rangle_\sigma = \big\langle G_e\big[\psi_j^e\big], G_e\big[\psi_{j'}^e\big]\big\rangle_\sigma = \big\langle G_e^* G_e\big[\psi_j^e\big], \psi_{j'}^e\big\rangle. \tag{51}$$

Proposition 4.1. *For any $\epsilon > 0$ using the grid in the Fourier domain described in proposition 3.1 yields $\|G_e^* G_e - F_e^* F_e\|_2 \leqslant \epsilon$, where $\|\cdot\|_2$ is the norm induced by the inner product (11).*

Proof. From (15),

$$(F_e^* F_e)_{mn,m'n'} = \frac{1}{N^2} K_{\pi N}\big(\mathbf{x}_{mn}^e - \mathbf{x}_{m'n'}^e\big)$$

and using (49) with σ_k, $\mathbf{p}_{kl}$ in proposition 3.1 for ϵ, we have that all entries of $G_e^* G_e - F_e^* F_e$ are bounded by ϵ/N^2. Thus, the result follows. □

The eigenvectors $\psi_j^{\sharp,e}$ are almost orthonormal. In fact,

Proposition 4.2. *For ϵ in proposition 3.1, we have*

$$\left|\left\langle \psi_j^{\sharp,e}, \psi_{j'}^{\sharp,e}\right\rangle_\sigma - \mu_j^e \delta_{jj'}\right| \leqslant \epsilon,$$

for all $j, j' = 0, \ldots, N^2 - 1$.

Therefore, the images of eigenvectors $\left\{\psi_j^e\right\}_{j=0}^{N^2-1}$ in the Fourier domain, $\left\{\psi_j^{\sharp,e}\right\}_{j=0}^{N^2-1}$, are approximately orthogonal and we will use them as a basis.

Proof. The eigenvectors ψ_j^e of (16) are orthonormal (17). Using (50) and (51),

$$\left\langle \psi_j^{\sharp,e}, \psi_{j'}^{\sharp,e}\right\rangle_\sigma - \mu_j^e \delta_{jj'} = \left\langle G_e^* G_e \psi_j^e, \psi_{j'}^e\right\rangle - \left\langle F_e^* F_e \psi_j^e, \psi_{j'}^e\right\rangle = \left\langle \left(G_e^* G_e - F_e^* F_e\right) \psi_j^e, \psi_{j'}^e\right\rangle,$$

we arrive at

$$\left|\left\langle \psi_j^{\sharp,e}, \psi_{j'}^{\sharp,e}\right\rangle_\sigma - \mu_j^e \delta_{jj'}\right| \leqslant \left\| G_e^* G_e - F_e^* F_e \right\|_2 \left\| \psi_j^e \right\|_2 \left\| \psi_{j'}^e \right\|_2 \leqslant \epsilon,$$

using proposition 4.1. □

4.2. Unequally spaced discretization in the spatial domain

Similarly, we introduce the discrete versions of (22) and (23) as

$$\begin{aligned} &G_{\omega,2c} : \mathbb{C}_\omega^{N_\omega^2} \to \mathbb{C}_\sigma^{N_\sigma} \\ &f_\omega^\sharp(\mathbf{p}_{kl}) = G_{\omega,2c}[\mathbf{f}](\mathbf{p}_{kl}) = \sum_{m,n=0}^{N_\omega - 1} \omega_{mn} f\left(\mathbf{x}_{mn}^\omega\right) \mathrm{e}^{-\mathrm{i}2c\mathbf{p}_{kl}\cdot\mathbf{x}_{mn}^\omega}, \end{aligned} \tag{52}$$

and its adjoint transform

$$\begin{aligned} &G_{\omega,2c}^* : \mathbb{C}_\sigma^{N_\sigma} \to \mathbb{C}_\omega^{N_\omega^2} \\ &G_\omega^*[g]\left(\mathbf{x}_{mn}^p\right) = \sum_{kl} \sigma_k g(\mathbf{p}_{kl}) \, \mathrm{e}^{\mathrm{i}2c\mathbf{p}_{kl}\cdot\mathbf{x}_{mn}^\omega}, \end{aligned} \tag{53}$$

where $\mathbf{p}_{kl}$ and σ_{kl} are given by proposition 3.1, N_σ is the total number of nodes $\mathbf{p}_{kl}$, $\mathbf{x}_{mn}^p$ is given by (19) and ω_{mn} is given by (20). The inner products $\langle\cdot\rangle_\omega$ and $\langle\cdot\rangle_\sigma$ are defined in (21) and (46) respectively. The matrix elements of $G_{\omega,2c}^* G_{\omega,2c}$ are given by

$$(G_{\omega,2c}^* G_{\omega,2c})_{mn,m'n'} = \sum_{kl} \sigma_k \, \mathrm{e}^{\mathrm{i}2c\mathbf{p}_{kl}\cdot\left(\mathbf{x}_{mn}^\omega - \mathbf{x}_{m'n'}^\omega\right)} \omega_{m'n'}. \tag{54}$$

Let us denote by $\psi_j^\omega = \left\{\psi_j^\omega\left(\mathbf{x}_{mn}^\omega\right)\right\}_{m,n=0}^{N_\omega - 1}$ an eigenvector of (27) and define by

$$\psi_j^{\sharp,\omega}(\mathbf{p}_{kl}) = G_{\omega,2c}\left[\psi_j^\omega\right] \tag{55}$$

its image in the Fourier domain.

We obtain

$$\left\langle \psi_j^{\sharp,\omega}, \psi_{j'}^{\sharp,\omega}\right\rangle_\sigma = \left\langle G_{\omega,2c}\left[\psi_j^\omega\right], G_{\omega,2c}\left[\psi_{j'}^\omega\right]\right\rangle_\sigma = \left\langle G_{\omega,2c}^* G_{\omega,2c}\left[\psi_j^\omega\right], \psi_{j'}^\omega\right\rangle_\omega.$$

Proposition 4.3. *For any $\epsilon > 0$, the grid in the Fourier domain described in proposition 3.1 yields $\|G_{\omega,2c}^* G_{\omega,2c} - F_{\omega,2c}^* F_{\omega,2c}\|_\omega \leqslant \epsilon \sum_{m,n=0}^{N_\omega - 1} \omega_{mn}$, where $\|\cdot\|_\omega$ is the norm induced by the inner product (21).*

Proof. Let us consider the matrix A given by $A = G_{\omega,2c}^* G_{\omega,2c} - F_{\omega,2c}^* F_{\omega,2c}$. This matrix is Hermitian with respect to the inner product in (21), so that the induced matrix norm $\|A\|_\omega$ is

$$\|A\|_\omega = \sup_{\|f\|_\omega = 1} \left|\langle Af, f\rangle_\omega\right|$$

for vectors $f \in \mathbb{C}^{N_\omega^2}_\omega$. Using (24), (54) and proposition 3.1, we interpret the matrix A as $A = EW$, where all entries $e_{mn,m'n'}$ of E are less than ϵ and W is the diagonal matrix with positive entries ω_{mn}. Thus, we have

$$|\langle EWf, f\rangle_\omega| = \left|\sum_{mn}\sum_{m'n'} e_{mn,m'n'}\omega_{m'n'} f_{m'n'}\omega_{mn}\bar{f}_{mn}\right| \leqslant \epsilon \left|\sum_{mn}\omega_{mn} f_{mn}\right|^2,$$

and, using the Cauchy–Schwarz inequality,

$$\left|\sum_{mn}\omega_{mn}^{1/2}\omega_{mn}^{1/2} f_{mn}\right|^2 \leqslant \left(\sum_{mn}\omega_{mn}\right)\|f\|_\omega^2,$$

we obtain the result. □

Remark 4.1. From (18), with $y = 0$, we have $\left|\sum_{m=0}^{N_\omega-1}\omega_m - 2\right| \leqslant \epsilon_\omega$. Therefore, from definition (20) it follows that the constant $\sum_{m,n=0}^{N_\omega-1}\omega_{mn}$ is close to 1.

The eigenvectors $\psi_j^{\sharp,\omega}$ are almost orthonormal as is stated in

Proposition 4.4. *For ϵ in proposition 3.1, we have*

$$\left|\left\langle\psi_j^{\sharp,\omega}, \psi_{j'}^{\sharp,\omega}\right\rangle_\sigma - \mu_j^\omega\delta_{jj'}\right| \leqslant \epsilon\sum_{m,n=0}^{N_\omega-1}\omega_{mn},$$

for all $j, j' = 0, \ldots, N_\omega^2 - 1$.

Therefore, the images of eigenvectors $\left\{\psi_j^\omega\right\}_{j=0}^{N_\omega^2-1}$ in the Fourier domain, $\left\{\psi_j^{\sharp,\omega}\right\}_{j=0}^{N_\omega^2-1}$, are approximately orthogonal and we will use them as a basis.

Proof. The eigenvectors ψ_j^ω of (27) are orthonormal (28). Using (55) and (51),

$$\begin{aligned}\left\langle\psi_j^{\sharp,\omega}, \psi_{j'}^{\sharp,\omega}\right\rangle_\sigma - \mu_j^\omega\delta_{jj'} &= \left\langle G_{\omega,2c}^* G_{\omega,2c}\psi_j^\omega, \psi_{j'}^\omega\right\rangle - \left\langle F_{\omega,2c}^* F_{\omega,2c}\psi_j, \psi_{j'}^\omega\right\rangle \\ &= \left\langle\left(G_{\omega,2c}^* G_{\omega,2c} - F_{\omega,2c}^* F_{\omega,2c}\right)\psi_j^\omega, \psi_{j'}^\omega\right\rangle,\end{aligned}$$

we arrive at

$$\left|\left\langle\psi_j^{\sharp,\omega}, \psi_{j'}^{\sharp,\omega}\right\rangle_\omega - \mu_j^\omega\delta_{jj'}\right| \leqslant \left\|G_{\omega,2c}^* G_{\omega,2c} - F_{\omega,2c}^* F_{\omega,2c}\right\|_\omega \left\|\psi_j^\omega\right\|_\omega \left\|\psi_{j'}^\omega\right\|_\omega \leqslant \epsilon\sum_{m,n=0}^{N_\omega^2-1}\omega_{mn},$$

using proposition 4.3. □

5. Inverse discrete transform

Since the discrete transforms G_e and $G_{\omega,2c}$ in (47) and (52) are not unitary, inverting them requires, in general, solving a system of linear equations which, due to ill conditioning, typically requires additional constraints or modifications (see remark 5.2). However, there are important cases where solving such a system may be avoided. In particular, if a function is sufficiently oversampled so that (up to specified accuracy) the essential support of $\hat{f}$ is contained within D_{2c}, the inversion may be accomplished by simply using the adjoint transforms in (48) and (53).

It is important to point out differences between the transforms G_e and $G_{\omega,2c}$ (or F_e and $F_{\omega,2c}$). The intended use of these transforms assumes different conditions when we apply them to a function in the spatial domain B. For the transform G_e, we assume that (within

the required precision) the function is smooth and periodic in the square B. This is similar to the requirements on a function for using the DFT to approximate its Fourier transform. In this case, we require the function to be approximately periodic and sampled with at least the Nyquist rate. These conditions assure that trigonometric interpolation may be performed without the artifact of Gibbs phenomenon. Since most signals are not periodic, they are periodized by applying a window; an extensive literature is devoted to constructing algorithms for this purpose. Effectively, the only difference between the discrete transform G_e and the DFT is the grid used in the Fourier domain. If a smooth function is periodic in B and is oversampled above the Nyquist rate by a factor of at least $\sqrt{2}$, then its support in the Fourier domain will be (essentially) within the disk D_{2c}. As a result, to invert G_e it is sufficient to apply the adjoint transform (48).

On the other hand, for the transform $G_{\omega,2c}$ (or $F_{\omega,2c}$) we no longer require the smooth function to be periodic in B. However, removing the periodicity constraint requires the introduction of the unequally spaced grid in the spatial domain (19). As one would expect, the number of grid points exceeds the Nyquist sampling rate for periodic functions, but the extra factor (described in [8, 9] for functions on an interval) approaches 1 as the number of points becomes large. We note that by selecting the classical, polynomial-based quadrature nodes, the oversampling factor asymptotically approaches $\pi/2$.

If a smooth function in B is not periodic, its Fourier transform $\hat{f}(p_1, p_2)$ in (4) decays asymptotically as $1/\sqrt{p_1^2 + p_2^2}$ and, thus, the support of $\hat{f}$ is not limited to the disk D_{2c}. Yet, as we describe below, it is possible to recover the function f if it belongs (within the desired precision) to a subspace generated by eigenvectors in (27) with eigenvalues above a selected threshold. The algorithm exploits the structure of the spectrum of $Q_{\omega,2c}$ in (27), namely, the fact that most eigenvalues concentrate near one or zero, leaving only $\mathcal{O}(\log N_\omega)$ eigenvalues in the decay region. In our inversion algorithm, we avoid solving a linear system by computing in advance the $\mathcal{O}(\log N_\omega)$ eigenvectors corresponding to the decay region. With this provision, the algorithm requires only $\mathcal{O}\big(N_\omega^2 \log N_\omega\big)$ operations.

We start by expanding the function values $\mathbf{f}$ with respect to the eigenvectors ψ_j^ω in (27),

$$\mathbf{f} = \sum_{j=0}^{N_\omega^2-1} \big\langle \mathbf{f}, \psi_j^\omega \big\rangle_\omega \psi_j^\omega. \tag{56}$$

In order to describe the inversion algorithm for a given accuracy $\delta > 0$, let us split the spectrum of $Q_{\omega,2c}$ into three parts and define the corresponding sets of indices as $J_{\text{head}} = \big\{ j \in \mathbb{N} \big| \mu_j^\omega > 1-\delta \big\}$, $J_{\text{decay}} = \big\{ j \in \mathbb{N} \big| 1-\delta \geqslant \mu_j^\omega \geqslant \delta \big\}$ and $J_{\text{tail}} = \big\{ j \in \mathbb{N} \big| \mu_j^\omega < \delta \big\}$.

We assume that the vector $\mathbf{f}$ has a small projection on the eigenvectors of the tail region,

$$\left(\sum_{j \in J_{\text{tail}}} \big| \big\langle \mathbf{f}, \psi_j^\omega \big\rangle_\omega \big|^2 \big(1 - \mu_j^\omega\big)^2 \right)^{1/2} \leqslant \delta \|\mathbf{f}\|_\omega. \tag{57}$$

Since $\mu_j^\omega \leqslant \delta$ for $j \in J_{\text{tail}}$, condition (57) effectively requires that the tail portion of the function has a small relative norm. Since for small μ_j^ω the essential support of the Fourier transform of ψ_j^ω is outside the disk D_{2c}, it is a natural condition to impose.

Given $\mathbf{f}^\sharp = G_{\omega,2c}[\mathbf{f}]$, where $G_{\omega,2c}$ is the forward transform (52), we would like to recover $\mathbf{f}$ under the assumption (57). Let us describe the algorithm where we assume that the functions ψ_j^ω and $\psi_j^{\sharp,\omega}$ for indices $j \in J_{\text{decay}}$ have been computed in advance.

(i) We start by computing projections

$$\alpha_j = \big\langle \mathbf{f}^\sharp, \psi_j^{\sharp,\omega} \big\rangle_\sigma, \tag{58}$$

for indices in J_{decay}. The cost of this computation is $\mathcal{O}(N_\sigma \log N_\omega)$.

(ii) Given the projection coefficients α_j and the eigenvalues μ_j^ω, we form

$$\mathbf{d} = \sum_{j \in J_{\text{decay}}} \frac{\alpha_j}{\mu_j^\omega} \psi_j^\omega$$

and

$$\mathbf{d}^\sharp = \sum_{j \in J_{\text{decay}}} \frac{\alpha_j}{\mu_j^\omega} \psi_j^{\sharp,\omega}.$$

This requires $\mathcal{O}\big(N_\omega^2 \log N_\omega\big)$ and $\mathcal{O}(N_\sigma \log N_\omega)$ operations. We note that $G_{\omega,2c}(\mathbf{d}) = \mathbf{d}^\sharp$.

(iii) As an approximation to $\mathbf{f}$, we compute

$$\mathbf{f}_{\text{recon}} = G^*_{\omega,2c}[\mathbf{f}^\sharp - \mathbf{d}^\sharp] + \mathbf{d}. \tag{59}$$

The application of $G^*_{\omega,2c}$ requires $\mathcal{O}(N_\sigma \log N_\sigma) + \mathcal{O}\big(N_\omega^2 \log N_\omega\big)$ operations via the USFFT. Note that N_σ is proportional to N_ω^2.

To show why $\mathbf{f}_{\text{recon}}$ in (59) is a reasonable approximation to $\mathbf{f}$, we split $\mathbf{f}$ in (56) as $\mathbf{f} = \mathbf{f}_{\text{head}} + \mathbf{f}_{\text{decay}} + \mathbf{f}_{\text{tail}}$ with indices in corresponding sets, J_{head}, J_{decay} and J_{tail}. We note that G^*_ω acts as an approximate inverse on $\mathbf{f}_{\text{head}}$ since the eigenvalues in J_{head} are close to 1 and the contribution from $\mathbf{f}_{\text{tail}}$ is negligible due to the assumption (57). The remaining contribution $\mathbf{f}_{\text{decay}}$ is computed explicitly. We quantify this statement in

Theorem 5.1. *For a given $\delta > 0$ and $\epsilon > 0$ in proposition 3.1, consider a vector $\mathbf{f}$ satisfying (57). Then, given $\mathbf{f}^\sharp = G_\omega[\mathbf{f}]$, we compute $\mathbf{f}_{\text{recon}}$ via (59) as an approximation to $\mathbf{f}$ so that*

$$\|\mathbf{f} - \mathbf{f}_{\text{recon}}\|_\omega \leqslant (2\delta + \epsilon C_\omega C_\mu + 2\epsilon C_\omega + \epsilon^2 C_\omega^2 \tilde{C}_\mu) \|\mathbf{f}\|_\omega, \tag{60}$$

where

$$C_\mu = C_\mu(\delta) = \left(\sum_{j \in J_{\text{decay}}} \left(\frac{1 - \mu_j^\omega}{\mu_j^\omega} \right)^2 \right)^{1/2}, \qquad \tilde{C}_\mu = \tilde{C}_\mu(\delta) = \left(\sum_{j \in J_{\text{decay}}} \left(\frac{1}{\mu_j^\omega} \right)^2 \right)^{1/2}$$

and

$$C_\omega = \sum_{m,n=0}^{N_\omega - 1} \omega_{mn}.$$

The proof of this theorem is presented in appendix A.3.

Remark 5.1. The same result and estimates hold for the transform G_e. We also note that in both cases, if the projection on the eigenvectors with indices in J_{decay} are negligible, then these algorithms amount to the application of the adjoint transform.

For selected δ, in our algorithm we choose $\epsilon \approx \delta^2$. Recall that ϵ only affects the choice of the Fourier grid via proposition 3.1. The additional cost to achieve greater accuracy, e.g. from ϵ to ϵ^2, is insignificant since we only need to add a small number of nodes, $\mathcal{O}(\log \epsilon^{-1})$ (see remark 3.1). We have both $C_\mu(\delta) \approx 1/\delta$ and $\tilde{C}_\mu(\delta) \approx 1/\delta$, so that the estimate (60) yields

$$\frac{\|\mathbf{f} - \mathbf{f}_{\text{recon}}\|_\omega}{\|\mathbf{f}\|_\omega} = \mathcal{O}(\delta). \tag{61}$$

Remark 5.2. In the case of non-unitary transform pairs G and G^* (e.g., $G_{\omega,2c}$ and $G^*_{\omega,2c}$ or G_e and G_e^*) the usual approach to find f given $g = Gf$ is to form the normal system $G^*Gf = G^*g$. Since such a linear system is ill conditioned (see figure 1), in order to apply an

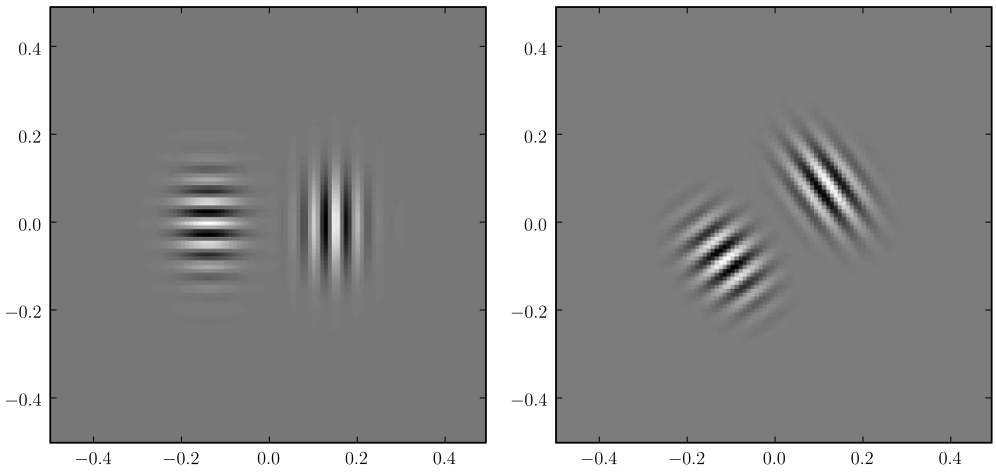

Figure 4. Rotation of function (62) by $\phi = \pi/5$.

iterative procedure for finding f, e.g. the conjugate gradient method, a typical modification is to solve $(G^*G + \delta I) f = G^* g$, with some δ. Although such an approach is applicable here, it only offers indirect control over the accuracy and is a rather slow algorithm since the number of iterations depends on the condition number of the normal system (of order $\mathcal{O}(\delta^{-1})$). On the other hand, the algorithm of this section is of the same complexity as the transforms G and G^* and does not require solving a linear system.

Remark 5.3. In contrast to our construction, Slepian's disk to disk mapping [23] has $\mathcal{O}(N_\omega \log N_\omega)$ eigenvalues in the decay region (out of a total of N_ω^2). The reason for this large proportion is that variables separate and, for a fixed angular mode, each radial component contributes $\mathcal{O}(\log N_\omega)$ eigenvalues to the decay region [22]. Thus, the inversion algorithm of this section is not available in the original Slepian's setup.

6. Examples

6.1. Rotation of smooth space-limited signals

Using the grid in proposition 3.1 yields a simple algorithm for rotating signals by an arbitrary angle, provided that these signals are effectively periodic in space and band-limited in the Fourier domain with sufficient accuracy (see section 5). In this case, we may use the adjoint transform G_e^* in lieu of the inverse. The algorithm consists of applying G_e in (47), rotating the grid in proposition 3.1 by the selected angle ϕ, and applying G_e^* in (48) with the rotated grid.

We demonstrate this algorithm using

$$f(x_1, x_2) = \mathrm{e}^{-\sigma_1 (x_1 - \tau)^2} \mathrm{e}^{-\sigma_2 x_2^2} \cos(k x_1) + \mathrm{e}^{-\sigma_1 (x_1 + \tau)^2} \mathrm{e}^{-\sigma_2 x_2^2} \cos(k x_2), \tag{62}$$

where $k = 40\pi, \sigma_1 = 240, \sigma_2 = 100$ and $\tau = 1/7$. We are given the samples $f_{mn} = f\left(-\frac{1}{2} + \frac{m}{N}, -\frac{1}{2} + \frac{n}{N}\right)$ with $m, n = 0, \ldots, N-1$ and $N = 110$. The result of rotating by an angle $\phi = \pi/5$ is illustrated in figure 4. In this example, the grid in the Fourier domain was constructed with $\epsilon \approx 6.38 \times 10^{-12}$ in proposition 3.1. The absolute deviation of the result of rotation (from the exact values) is 1.33×10^{-11}. We note that this example also illustrates the use of the adjoint as an inverse (rotation by $\phi = 0$) given that the function f is

well localized in square B and is oversampled so that its Fourier transform is well localized in D_{2c}. We note that this function projects on the eigenvectors of (16) with the eigenvalues close to 1.

6.2. *Fourier transform of smooth, non-periodic functions*

Although the transform $G_{\omega,2c}$ may appear similar to G_e, it is quite different in that it allows us to work with smooth, non-periodic functions in the square B. Since the Fourier coefficients of such functions decay slowly, we use the analysis introduced by Slepian *et al* [23–26] and the transforms in (52) and (53) providing a discrete version for such an approach. The following example uses the approach described in section 5 and shows that we can work with smooth, non-periodic functions, something that is not directly possible by using the ordinary DFT.

We consider a function

$$f(x_1, x_2) = \begin{cases} e^{i(k_1 x_1 + k_2 x_2)} & (x_1, x_2) \in B \\ 0 & \text{otherwise} \end{cases} \tag{63}$$

with $k_1 = 11\pi$, $k_2 = 3\pi$ and its Fourier transform

$$\hat{f}(\xi_1, \xi_2) = \frac{4 \sin\left(\frac{k_1}{2} - \pi\xi_1\right) \sin\left(\frac{k_2}{2} - \pi\xi_2\right)}{(k_1 - 2\pi\xi_1)(k_2 - 2\pi\xi_2)} \tag{64}$$

on the grid $\mathbf{p}_{kl}$ in proposition 3.1 with $c = 12.5$ and $\epsilon \approx 4.9 \times 10^{-6}$. Given the values of the function (64), $\hat{\mathbf{f}} = \{\hat{f}(\mathbf{p}_{kl})\}_{k,l}$, we reconstruct the function f in (63) on the grid given in (19) with $N_\omega = 60$. The accuracy of such a reconstruction is estimated in theorem 5.1. Choosing $\delta \approx 3.16 \times 10^{-6}$, we compute

$$\left(\sum_{j \in J_{\text{tail}}} \left| \langle \mathbf{f}, \psi_j^\omega \rangle_\omega \right|^2 \left(1 - \mu_j^\omega\right)^2 \right)^{1/2} \approx 1.25 \times 10^{-4}.$$

We then use the inversion algorithm described in section 5 and compare the result with exact values of f in (63). We obtain

$$\|\mathbf{f}_{\text{recon}} - \mathbf{f}\|_\omega \approx 1.25 \times 10^{-4},$$

and the reconstruction and its error are illustrated in figure 5. We note that the reconstructed component on the subspace corresponding to the decay region is mostly supported near the boundary. For comparison, the accuracy of inverting using only the adjoint transform is $\|G^*_{\omega,2c}\hat{\mathbf{f}} - \mathbf{f}\|_\omega \approx 6.48 \times 10^{-2}$.

7. Double integrals over spheres

Although grids in proposition 3.1 are efficient and useful, it is often desirable to build grids with emphasis on other properties. In what follows, we construct grids (and associated fast algorithms) suggested by integrals arising in linearized scattering problems. For a function in $\mathbb{R}^d$, band-limited in a ball of radius $2c$,

$$f_{2c}(\mathbf{x}) = \frac{1}{(2\pi)^d} \int_{D_{2c}} \hat{f}_{2c}(\mathbf{p})\, e^{i\mathbf{p}\cdot\mathbf{x}}\, d\mathbf{p}, \tag{65}$$

it has been shown in [5, 6, 10, 13] that it may be written as a double integral over spheres,

$$f_{2c}(\mathbf{x}) = \frac{c^d}{2^{(d+2)/2}\pi^d \Omega_{d-1}} \int_{|\mu|=1} \int_{|\nu|=1} \hat{f}_{2c}(c\mu - c\nu)\, e^{i(c\mu - c\nu)\cdot\mathbf{x}} w(\mu \cdot \nu)\, d\mu\, d\nu, \tag{66}$$

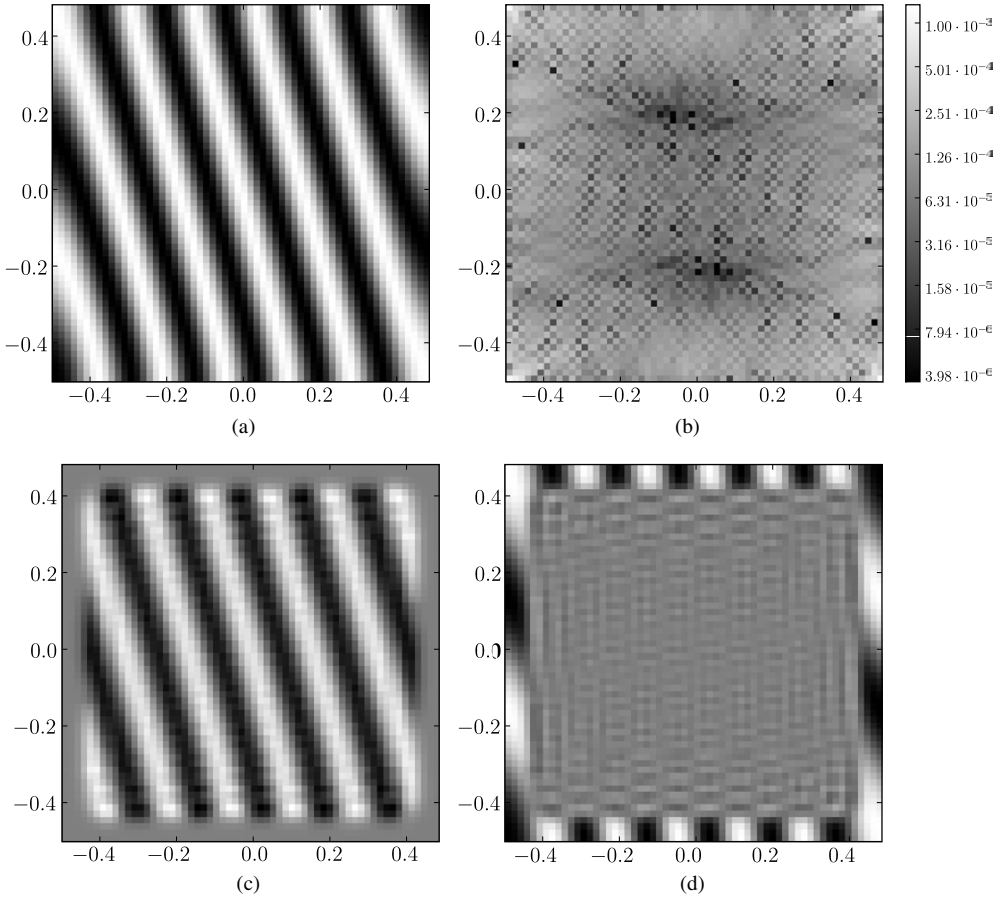

Figure 5. (a) The real part of the function f in (63) and the two components of its reconstruction via algorithm in section 5, where (c) is $G^*_{\omega,2c}[\mathbf{f}^\sharp - \mathbf{d}^\sharp]$ and (d) is $\mathbf{d}$ in (59). The contribution from $\mathbf{d}$ is mostly near the boundary and the sum of (c) and (d) yields (a) with accuracy $\|\mathbf{f}_{\text{recon}} - \mathbf{f}\|_\omega \approx 1.25 \times 10^{-4}$. The spatial distribution of the error is shown in (b). Note that maximum error occurs in the corners.

where μ and ν are unit vectors in $\mathbb{R}^d$,

$$w(\mu \cdot \nu) = \frac{(1 - \mu \cdot \nu)^{1/2}}{(1 + \mu \cdot \nu)^{(d-3)/2}},$$

and $\Omega_d = 2\pi^{d/2}/\Gamma(d/2)$ is the surface area of the unit sphere in $\mathbb{R}^d$. In linearized inverse problems, the scattering amplitude is measured as $\hat{f}_{2c}(c\mu - c\nu)$, where the unit vectors represent the incident and scattering directions (see e.g. [5, 6, 10, 13]). The integral (66) follows from a general relation for iterated spherical means (see [5, 16]) and has been of practical interest in dimensions $d = 2, 3$.

In this paper we use (66) for $d = 2$,

$$f_{2c}(\mathbf{x}) = \frac{c^2}{8\pi^2} \int_{|\mu|=1} \int_{|\nu|=1} \hat{f}_{2c}(c\mu - c\nu)\, \mathrm{e}^{\mathrm{i}(c\mu - c\nu)\cdot\mathbf{x}} [1 - (\mu \cdot \nu)^2]^{1/2}\, \mathrm{d}\mu\, \mathrm{d}\nu, \tag{67}$$

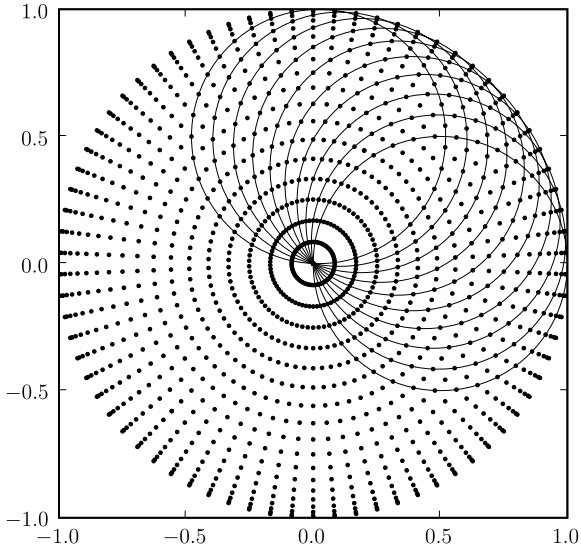

Figure 6. An equally spaced discretization in angles α and β for $N_\alpha = N_\beta = 37$. Note that the points align themselves on diameters although they are constructed using rotating circles.

where $\mathbf{x} = (x_1, x_2)$. Writing unit vectors $\mu = (\cos\alpha, \sin\alpha)$ and $\nu = (\cos\beta, \sin\beta)$, we have

$$f_{2c}(\mathbf{x}) = \frac{c^2}{8\pi^2}\int_0^{2\pi}\int_0^{2\pi} \tilde{f}(\alpha,\beta)\, \mathrm{e}^{\mathrm{i}c(x_1[\cos(\alpha)-\cos(\beta)]+x_2[\sin(\alpha)-\sin(\beta)])}|\sin(\alpha-\beta)|\,\mathrm{d}\alpha\,\mathrm{d}\beta, \tag{68}$$

where $\tilde{f}(\alpha,\beta) = \hat{f}_{2c}(c(\cos\alpha - \cos\beta), c(\sin\alpha - \sin\beta))$. The function $\tilde{f}(\alpha,\beta)$ is a smooth, periodic function in the variables α and β, thus permitting accurate trigonometric interpolation, as described below. Due to the range of these variables, the disk D_{2c} is covered twice.

Using an equally spaced grid in angles α and β to discretize $\tilde{f}(\alpha,\beta)$, we set

$$\alpha_l = \frac{2\pi l}{N_\alpha}, \qquad \beta_{l'} = \frac{2\pi l'}{N_\beta} \tag{69}$$

and

$$u_{ll'} = \frac{\cos\alpha_l - \cos\beta_{l'}}{2}, \qquad v_{ll'} = \frac{\sin\alpha_l - \sin\beta_{l'}}{2}, \tag{70}$$

so that $|u_{ll'}| \leqslant 1$, $|v_{ll'}| \leqslant 1$ and

$$\tilde{f}_{ll'} = \hat{f}_{2c}(2cu_{ll'}, 2cv_{ll'}), \tag{71}$$

where $l = 0, \ldots, N_\alpha - 1$ and $l' = 0, \ldots, N_\beta - 1$. This discretization is illustrated in figure 6 where, somewhat unexpectedly, the grid points line up on the diameters of the disk although they were generated using (70). This is further illustrated in figure 7.

Let us choose $L = N_\alpha = N_\beta$ so that

$$\alpha_l = \frac{2\pi l}{L}, \qquad \beta_{l'} = \frac{2\pi l'}{L}, \qquad l, l' = 0, \ldots, L-1. \tag{72}$$

Then, the Fourier grid points can be written as

$$(u_{ll'}, v_{ll'}) = \sin\frac{\alpha_l - \beta_{l'}}{2}\left(-\sin\frac{\alpha_l + \beta_{l'}}{2}, \cos\frac{\alpha_l + \beta_{l'}}{2}\right), \tag{73}$$

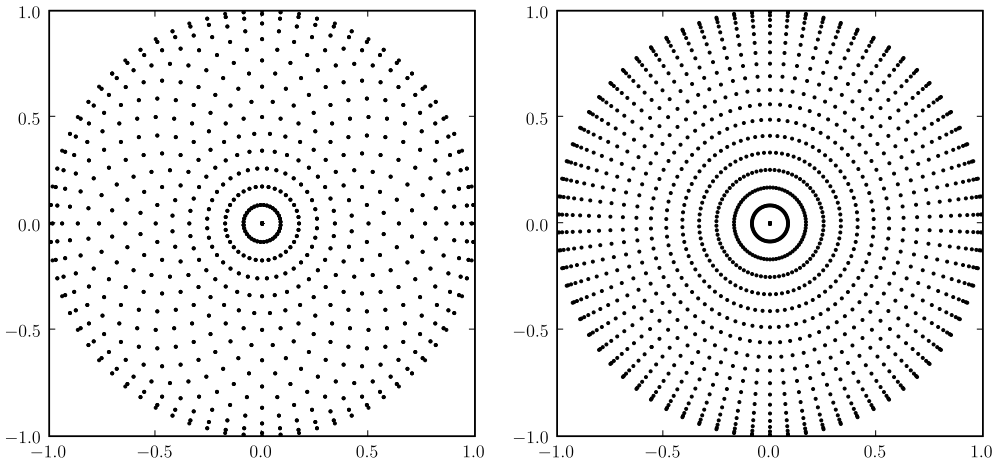

Figure 7. Grids with even $N_\alpha = N_\beta = 36$ (a) and odd $N_\alpha = N_\beta = 37$ (b) number of points in the subdivision.

where

$$\frac{\alpha_l - \beta_{l'}}{2} = \frac{\pi(l - l')}{L} \qquad \text{and} \qquad \frac{\alpha_l + \beta_{l'}}{2} = \frac{\pi(l + l')}{L}.$$

For each fixed angle $\alpha_l - \beta_{l'}$, the grid points are located on a concentric circle with signed radius $\sin((\alpha_l - \beta_{l'})/2)$. For each fixed angle $\alpha_l + \beta_{l'}$, for example $\alpha_l + \beta_{l'} = 0$ and thus $l' = -l, l - l' = 2l$, the signed distance from zero to the grid points is $\sin\frac{1}{2}(\alpha_l - \beta_{l'}) = \sin(2\pi l/L)$. As l changes from 0 to $L - 1$ and L is odd, we generate all possible grid points for each fixed angle. These grid points along the diameters are illustrated in figure 6. We note that if L is even, then in our description in (73) some of the points coincide thus reducing the overall number of gridpoints (see below). Examples of both grids, for L even or odd, are plotted in figure 7.

By construction, the grids (72) with $N_\alpha = N_\beta = L$ are invariant under discrete rotation with the step size of the discretization. If we define

$$C^{\text{rot}}_{\alpha_l} = \left\{ \frac{1}{2}\left(\cos\alpha_l - \cos\beta_{l'}, \sin\alpha_l - \sin\beta_{l'}\right) \right\}_{l'=0,\ldots L-1}, \tag{74}$$

then, for each l, the grid points $C^{\text{rot}}_{\alpha_l}$ lie on a circle centered at $\frac{1}{2}(\cos\alpha_l, \sin\alpha_l)$ with radius $1/2$, as may be seen in figure 6.

Let us count the number of nodes in such grids for the case $N_\alpha = N_\beta = L$. If L is odd, then it follows from (73) that the grid points are located on concentric circles with signed distances given by

$$r_k = \cos\left(\frac{\pi}{2}\frac{2k+1}{L}\right), \qquad k = 0, 1, \ldots, L - 1. \tag{75}$$

We note that on each diameter the grid points described by (75) are (remarkably) the Chebyshev nodes on the interval $[-1, 1]$, zeros of $T_L(x) = 0$. Thus, we have $(L-1)/2$ concentric circles, each containing $2L$ grid points plus a single point at the origin. Therefore, we have a total of $L^2 - L + 1$ grid points.

If L is even, the grid points are located on concentric circles with signed distances given by

$$r_k = \cos\left(\pi \frac{k}{L}\right), \qquad k = 0, 1, \ldots, L-1, \tag{76}$$

which (with the exception of $r_0 = 1$) are zeros of the Chebyshev polynomial of the second kind $U_{L-1}(x) = 0$. Counting the number of grid points, we have $L/2$ concentric circles each containing L grid points and a single point at the origin, for a total of $L^2/2+1$ grid points. We note that the (almost) factor of two reduction of the number of points is due to the removal of double coverage in our description in (73); see figure 7.

We observe that using even L allows us to construct embedded grids of various resolutions as illustrated in figure 9. In this case, it is proper to consider such grids in space (see section 8) rather than Fourier domain.

7.1. Interpolation from the rotating grid

In contrast with the grids described in proposition 3.1, the grid in (72) does not directly lead to a high accuracy quadrature for integration of exponentials. However, it is an excellent grid for trigonometric interpolation along the circles $C^{\rm rot}_{\alpha_l}$, $l = 0, \ldots, L-1$, since the nodes on these circles are equally spaced. Therefore, using trigonometric interpolation, we first compute values of the function at points of intersection of the circles $C^{\rm rot}_{\alpha_l}$, $l = 0, \ldots, L-1$, and the concentric circles in proposition 3.1. We will explain how to choose L below.

The grids in proposition 3.1 lie on concentric circles C_{ρ_k} with radii ρ_k obtained in (30), namely,

$$C_{\rho_k} = \rho_k \{\cos\theta, \sin\theta\}_{\theta\in[0,2\pi)},$$

where $\rho_k > 0$, $k = \lfloor (M+1)/2 \rfloor + 1, \ldots, M$, and $\lfloor\rfloor$ denotes the integer part. These concentric circles intersect the circle $C^{\rm rot}_{\alpha_l}$ at points $\rho_k(\cos\gamma_{kl}, \sin\gamma_{kl})$, where the angles γ_{kl} may be found by solving

$$\cos(\gamma_{kl} - \alpha_l) = \rho_k \tag{77}$$

for each $l = 0, \ldots, L-1$, with α_l given by (69). For each fixed k and l there are two solutions of (77), γ_{kl} and $2\alpha_l - \gamma_{kl}$, as illustrated in figure 8(a). All intersection points γ_{kl} for all radii ρ_k and angles α_l are displayed in figure 8(b). We use only half of these points (on each concentric circle with radius ρ_k) leading to the grid in figure 8(c). This grid is one of the grids described in proposition 3.1. Indeed, these nodes are equally spaced in angle and their number is the same as the number of nodes in (34). This is illustrated in figure 8(d). The angular shift of the nodes does not impact the accuracy of the quadrature since these nodes simply provide an alternative discretization of the integral in proposition 3.1.

To interpolate on each circle $C^{\rm rot}_{\alpha_l}$ for fixed α_l, let us start with a set of values $\hat{f}_{l'} = \hat{f}(\beta_{l'})$ corresponding to the angles $\beta_{l'} = \frac{2\pi l'}{L}$ for $l' = 0, \ldots, L-1$ and compute the coefficients

$$f_n = \frac{1}{L} \sum_{l'=0}^{L-1} \hat{f}_{l'}\, \mathrm{e}^{\mathrm{i}\beta_{l'} n}, \tag{78}$$

where $n = 0, \ldots, L-1$. We then use the coefficients f_n for the trigonometric interpolation on the circle $C^{\rm rot}_{\alpha_l}$. We compute values $\tilde{\hat{f}}(\tilde{\beta}_k)$ for the angles $\tilde{\beta}_k = \gamma_{kl}$ that enumerate only the points that are used as quadrature nodes (see figure 8(c)). As explained above, the number of such nodes is $\lfloor (M+1)/2 \rfloor + 1$ and we have

$$\tilde{\hat{f}}(\tilde{\beta}_k) = \sum_{n=0}^{L-1} f_n\, \mathrm{e}^{-\mathrm{i}n\tilde{\beta}_k} \tag{79}$$

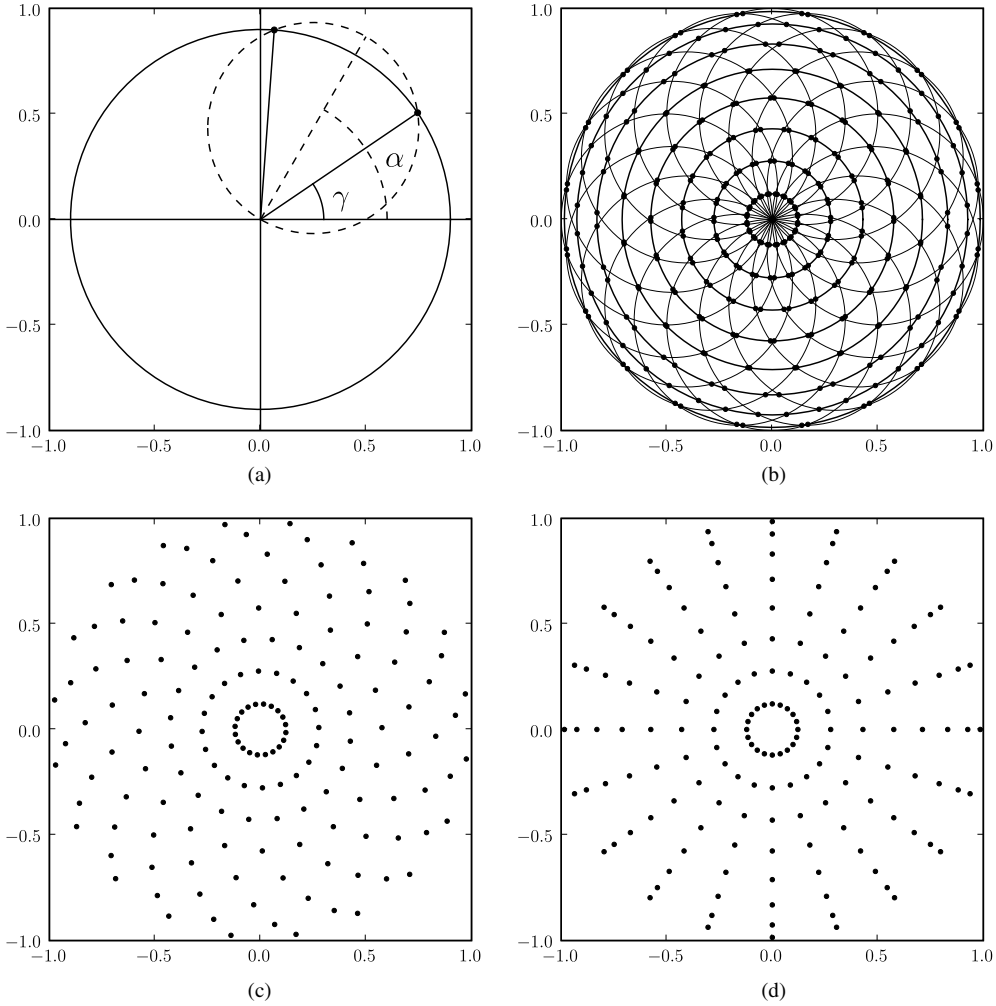

Figure 8. (a) Intersecting circles solving (77): a concentric circle C_ρ and a circle C_α^{rot} (indices are not displayed). (b) All intersections as solutions of (77) for $L = 20$. (c) Intersection points in (b) used as quadrature nodes. (d) A comparison with a grid equivalent to (c) vis-a-vis proposition 3.1 with nodes lying on diameters.

for $k = 0, \ldots, \lfloor (M+1)/2 \rfloor$. We use the FFT to compute (78) and the USFFT to compute (79) (see appendix A.2). We repeat this computation for each circle $C_{\alpha_l}^{\text{rot}}$; thus the total cost is $\mathcal{O}(L^2 \log L)$ operations.

For accurate trigonometric interpolation, we choose the number of nodes L to be the same (or larger) as the number of nodes on the concentric circle C_{ρ_k} with the largest radius ρ_k. Recall that the number of nodes is chosen in section 3 using (41) as the criterion; the selection of L follows the same derivation. In many cases, it is preferable to select even L as this reduces the overall number of nodes.

Our main point is that due to the trigonometric interpolation described above, the rotating grids of this section may be used in lieu of the near optimal grids of proposition 3.1. We point out additional applications of such rotating grids in section 8.

7.2. Example of interpolation from the rotating grid

Let us illustrate the accuracy of the trigonometric interpolation algorithm described in section 7.1. We transform a function from the spatial domain to the rotating grid in the Fourier domain given by (70). Next, we interpolate to the grid described in section 7.1. We then compare the resulting values in the Fourier domain with those computed directly from the function as well as with those computed analytically.

We use the function f in (63) from section 6.2. We set $\epsilon \approx 2.02 \times 10^{-15}$ and $N_\omega = 60$ resulting in $c = 10$. Let $(u_{ll'}, v_{ll'})$ be the rotating grid in (70) for $l, l' = 0, \ldots, L-1$, where L is given by (34) for a given accuracy and bandlimit. In this example, $L = 148$ and is the same as the number of grid points on the concentric circle of the largest radius in section 7.1. We compute the Fourier transform on the rotating grid $\hat{g}_{\rm rot} = \left\{G_{\omega,2c}[\mathbf{f}_\omega](u_{ll'}, v_{ll'})\right\}_{l,l'=0,\ldots,L-1}$, where $\mathbf{f}_\omega$ are the samples of f on the unequally spaced grid (19). We use the interpolation procedure to compute the values on the grid described in section 7.1 and denote the result as $\tilde{\hat{g}}_{\rm rot}$. We also compute directly the values on that grid

$$\hat{g} = \left\{G_{\omega,2c}[\mathbf{f}_\omega](\gamma_{kl})\right\}_{\substack{k=0,\ldots,\lfloor (M+1)/2\rfloor \\ l=0,\ldots,L-1}}.$$

The Fourier transform of the function is given in (64) and we denote by $\hat{f}$ its exact values on the same grid. We report the resulting errors:

- $\|\tilde{\hat{g}}_{\rm rot} - \hat{g}\|_\infty \approx 2.07 \times 10^{-14}$,
- $\|\tilde{\hat{g}}_{\rm rot} - \hat{f}\|_\infty \approx 1.86 \times 10^{-14}$, and
- $\|\hat{g} - \hat{f}\|_\infty \approx 8.88 \times 10^{-15}$, which we present for comparison.

This example demonstrates that the rotating grid may be used to achieve the same accuracy as the near optimal grid of proposition 3.1, whereas the grid points have the special property of being invariant under discrete rotations induced by the rotating circles.

8. Conclusion and remarks

In this paper, we have introduced grids and fast discrete transforms associated with functions band-limited in the disk. The grid described in section 3 provides accurate quadratures for band-limited functions, while the grid described in section 7 has other remarkable properties; we provide a fast algorithm to interpolate between them. The fast discrete transforms in section 4 are analogous to the DFT and their numerical implementation has the same complexity as the FFT. We also provide a fast inverse discrete transform in section 5 which utilizes properties of the eigenvectors and eigenvalues of the band-limiting and space-limiting operator constructed for our problem. We conclude with some remarks on applications and further work.

- The approach of this paper allows us to efficiently apply radial kernels in the Fourier domain. The necessary modification to accommodate a radial kernel with the Fourier transform $\hat{K}\left(\sqrt{p_1^2 + p_2^2}\right)$ (effectively band-limited in the disk D_{2c}) is to compute quadratures for the integral with the measure $\hat{K}(r)|r|\mathrm{d}r$ instead of the measure $|r|\mathrm{d}r$ used in this paper. It turns out that we do not need to require $\hat{K}$ to be positive and the approach in [8] allows us to construct an approximation

$$\left| \int_{-1}^{1} \hat{K}(r)|r| \mathrm{e}^{\mathrm{i}cr x}\, \mathrm{d}r - \sum_{m=1}^{M} w_m\, \mathrm{e}^{\mathrm{i}c\theta_m x} \right| \leqslant \epsilon.$$

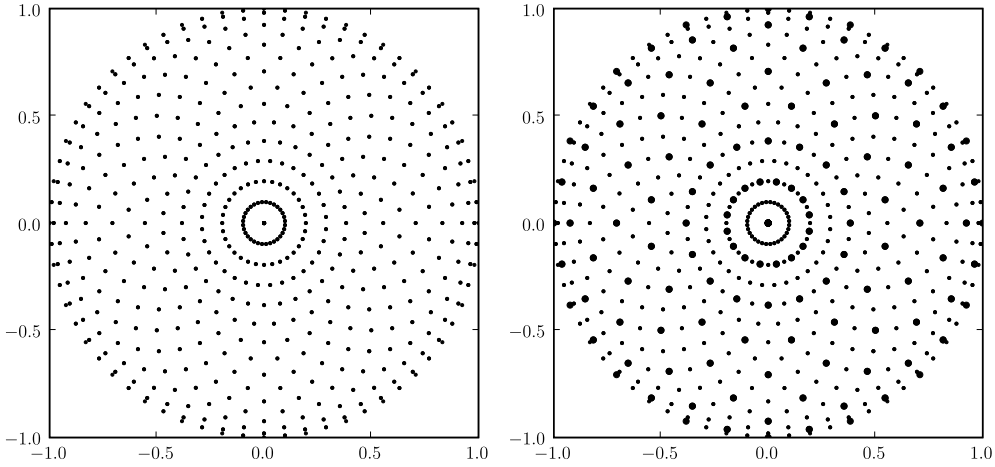

Figure 9. Embedded grids with $N_\alpha = N_\beta = 32$ and $N_\alpha = N_\beta = 16$.

Application of a convolution kernel is then obtained via a discrete transform that uses nodes generated by this approximate quadrature instead of the one in the paper. The details of such algorithms will be described elsewhere.

We note that the approach in [23] to construct the eigenfunctions, the PSWFs, relies on a commuting property of the relevant integral and differential operators. Such an approach is not available for a general measure $\hat{K}(r)|r|\mathrm{d}r$.

- The generalization of our results to dimension $d = 3$ requires quadratures for the measure $r^2\,\mathrm{d}r$ in the radial direction (easily handled by the approach in [8]) and an appropriate discretization of the sphere. The usual discretization of the sphere (via the equally spaced and the Legendre nodes), although workable, is not necessarily optimal or results in a grid with good invariant properties. For this reason, we plan to consider this case separately.
- Algorithms of this paper are applicable to problems of non-destructive evaluation, including x-ray tomography, MRI, electron microscopy and diffraction tomography. For MRI problems, our approach should result in a reduction of the data collection area in the Fourier domain as well as new algorithms for collecting data using the rotating grids of section 7. Since in any of such applications one needs to consider many specific details, we plan to address such problems separately.
- Although in this paper we consider disks in the Fourier domain, the same approach may be used to produce a grid for a disk in the spatial domain. We note that in such a case, we may use the multiresolution embedding of grids developed in section 7. This embedding is illustrated in figure 9. Such grids may be useful for discretizing and solving problems with, for example, cylindrical geometry.
- The polar transform in [3] has been used for constructing directional bases, the so-called curvelets [11]. Since our approach allows us to control accuracy, it is appropriate for constructing directional bases similar to constructions in [11], where we can incorporate additional useful features using Slepian's approach on radial wedges. We plan to develop such applications.
- The integral in (66) is not the most general formula of its kind (see [10]). In the general case, $\hat{f}(k_1\nu - k_2\mu)$ has support in the annulus with the outer radius $k_1 + k_2$ and the inner radius $k_1 - k_2$. It is also possible to extend (66) by integrating over the bandlimit

parameter, in addition to integrating over the two unit spheres [10]. We note that such generalizations may also serve as a starting point for useful discretizations.

- Nonlinear inversion algorithms for the Fourier transform that rely on the structure of the spectrum (see figure 1) are feasible within our overall approach and may provide more accurate results.

Acknowledgments

We would like to thank Bradley Alpert (NIST) for helpful suggestions to improve the original manuscript. This research was partially supported by NSF grant DMS-0612358, DOE/ORNL grant 4000038129 and AFOSR grant FA9550-07-1-0135.

Appendix A

A.1. Spectral properties of the operator $\mathcal{Q}_{2c}$

In this appendix, we briefly discuss properties of the spectrum of the operator $\mathcal{Q}_{2c}$. We show

Proposition A.1. *For any $c > 0$, all eigenvalues μ_j of the operator $\mathcal{Q}_{2c}$ belong to the open interval* $(0, 1)$.

Proof. To avoid carrying constants, in this proof we use the Fourier transform defined as a unitary operator,

$$\hat{g}(\mathbf{p}) = \int_{\mathbb{R}^2} g(\mathbf{x})\, \mathrm{e}^{-2\pi\, \mathrm{i}\mathbf{x}\cdot\mathbf{p}}\, \mathrm{d}\mathbf{x}.$$

Consider $g = \mathcal{Q}_{2c} f$, where the support of f is limited to the square B. The function g is naturally extended outside B to $\mathbb{R}^2$ by simply considering the integral defining g in $\mathbb{R}^2$. Note that such an extension cannot be identically zero outside B due to the compact support of its Fourier transform. Thus, we have

$$\|\mathcal{Q}_{2c} f\|_B < \|g\|_{L^2(\mathbb{R}^2)} = \|\hat{g}\|_{L^2(\mathbb{R}^2)} = \|\hat{f}\|_{D_{c/\pi}} \leqslant \|\hat{f}\|_{L^2(\mathbb{R}^2)} = \|f\|_B,$$

where we used the natural extension of the function f to $\mathbb{R}^2$. □

Let us show that the null space of $\mathcal{Q}_{2c}$ contains only zero, i.e. given that $\mathcal{Q}_{2c} f = 0$, we need to show that $f = 0$ in B. We define for $\mathbf{x} \in \mathbb{R}^2$,

$$g(\mathbf{x}) = \int_B K_{2c}(\mathbf{x} - \mathbf{y}) f(\mathbf{y})\, \mathrm{d}\mathbf{y} = \int_{\mathbb{R}^2} K_{2c}(\mathbf{x} - \mathbf{y}) f_B(\mathbf{y})\, \mathrm{d}\mathbf{y},$$

where f_B is zero outside the square B. Since the Fourier transform of the kernel is the characteristic function of a disk, we have

$$\hat{g}(\mathbf{p}) = \mathbf{1}_{D_{c/\pi}}(\mathbf{p})\, \hat{f}_B(\mathbf{p}),$$

implying that $\hat{g}(\mathbf{p}) = 0$ outside the disk in the Fourier domain. We have

$$g(\mathbf{x}) = \int_{D_{c/\pi}} \mathrm{e}^{2\pi\, \mathrm{i}\mathbf{p}\cdot\mathbf{x}} \hat{g}(\mathbf{p})\, \mathrm{d}\mathbf{p}$$

and consider $G(r) = g(r\hat{\mathbf{x}})$, where $\mathbf{x} = r\hat{\mathbf{x}}$, $\hat{\mathbf{x}}$ is a unit vector and $r \in \mathbb{R}$. We note that due to the compact support of $\hat{g}(\mathbf{p})$, $G(r)$ may be extended to an entire function of a complex variable, $G(z)$. Since $\mathcal{Q}_{2c} f = 0$, the function $G(z)$ is zero for $r\hat{\mathbf{x}} \in B$ and, therefore, vanishes identically as an entire function. Since $\hat{\mathbf{x}}$ is an arbitrary unit vector, we conclude that $g(\mathbf{x}) \equiv 0$

in $\mathbb{R}^2$. This, in turn, implies that $\hat{g}(\mathbf{p}) \equiv 0$ and, thus, $\hat{f}_B(\mathbf{p})$ is zero inside the disk $D_{c/\pi}$. Since f_B is compactly supported, by repeating the argument above, we conclude that $\hat{f}_B(\mathbf{p}) \equiv 0$ in the Fourier domain and, finally, $f_B \equiv 0$.

We also have

Proposition A.2. *For any c, the estimate $\|\mathcal{Q}_{2c}\|_B \leqslant c^2/\pi$ holds.*

We note that since we select $c = \pi N/2$, we have $c > \sqrt{\pi}$ for $N \geqslant 2$ and the norm bound $\|\mathcal{Q}_{2c}\|_B < 1$ is sharper.

Finally, in this paper we use that, asymptotically, most eigenvalues of $\mathcal{Q}_{2c}$ appear to concentrate near one or zero, leaving only $\mathcal{O}(\log N_\omega)$ eigenvalues in the transition region J_{decay} (see section 5). At the moment, we do not have a complete proof of this property; however, we have strong numerical evidence for it. We also note that this fact has been shown for PSWFs on an interval [23–26].

A.2. The unequally spaced fast Fourier transform

For speed the transforms of this paper rely on the USFFT developed in [7, 14] (also see [19, 20] and references therein). The USFFT evaluates trigonometric sums

$$h_n = \sum_{l=1}^{N_p} g_l \, \mathrm{e}^{\pm 2\pi \, \mathrm{i} N x_l \xi_n}, \qquad n = 1, \ldots N_f,$$

with accuracy ϵ and complexity $(C_1 N_p + C_2 N_f) \log \epsilon^{-1} + C_3 N \log N$. In dimension $d = 2$, these sums become

$$h_n = \sum_{l=1}^{N_p} g_l \, \mathrm{e}^{\pm 2\pi \, \mathrm{i}(N_x x_l \xi_n + N_y y_l \eta_n)}, \qquad n = 1, \ldots N_f,$$

and the algorithm has complexity $(\tilde{C}_1 N_p + \tilde{C}_2 N_f) \log \epsilon^{-1} + \tilde{C}_3 N_x N_y (\log N_x + \log N_y)$, where N_p is the number of points, N_f is the number of frequencies, $c = N\pi/2$, $c_x = N_x \pi/2$ and $c_y = N_y \pi/2$ are the corresponding bandlimits. Here we require that x_l, y_l, ξ_n and η_n are inside the interval $[-1/2, 1/2]$ but are otherwise arbitrary. This formulation is the most general.

The important special cases occur if

(i) frequencies are equally spaced, $N = N_f$, and $\xi_n = -\frac{1}{2} + n/N$, with $n = 0, \ldots, N-1$, or
(ii) points are equally spaced, $N = N_p$, and $x_l = -1/2 + l/N$, with $l = 0, \ldots, N-1$.

We note that although not explicitly described, the transform in the most general formulation is easily implied from algorithms described in [7]. The USFFT is also available in dimensions $d > 2$.

As stated above, the USFFT has the same complexity as the FFT; its speed differs from that of the FFT essentially by a factor (penalty factor below). For this reason it is useful to measure the speed of the USFFT in the units of the FFT on the same platform, thus providing some level of hardware-independent comparison. It should be noted that any reasonable algorithm based on local interpolation has the same complexity as the USFFT or, for this matter, the FFT (see e.g. [21]). The only difference between such algorithms is the penalty factor as a function of the desired accuracy. Unlike their predecessors, the algorithms developed in [7, 14] have controllable accuracy and a small penalty factor. The tight error estimates obtained in [7] make it possible to use these algorithms as 'off-the-shelf' tools (also see [19, 20]). We refer the reader to [7, 14, 19, 20] and references therein for timing information.

To give the reader a general idea of the speed, we note that the penalty factor (as compared to the FFT) in dimension 1 is roughly 2.5 − 8 and in dimension 2 is between 6 and 30 depending on accuracy requirements, type of the transform and implementation. There is an absolute lower limit on the penalty factor since all algorithms of this type use the FFT with oversampled data as a step of the computation. The oversampling factor is typically 4 (or 2 for the special cases) since these are more convenient factors to be used in conjunction with the FFT. Thus, the ultimate limit in performance has a penalty factor equal to the oversampling factor in dimension $d = 1$ and its square in dimension $d = 2$. We note that for low accuracies these oversampling factors can be made smaller and, thus, lead to faster algorithms than indicated here. We also note that except for separating the initialization step, we did not so far address a possible acceleration of the USFFT algorithms due to the specific grids employed in this paper.

A.3. Proof of theorem 5.1.

For brevity of notation, we drop the matrices dependence on c and write $F_\omega = F_{\omega,2c}$ and $G_\omega = G_{\omega,2c}$.

We first rewrite (59) as

$$\mathbf{f}_{\text{recon}} = G_\omega^* G_\omega[\mathbf{f} - \mathbf{d}] + \mathbf{d}$$

and obtain

$$\mathbf{f} - \mathbf{f}_{\text{recon}} = (I - G_\omega^* G_\omega)[\mathbf{f} - \mathbf{d}]. \tag{A.1}$$

Let us estimate $\|(I - G_\omega^* G_\omega)\mathbf{g}\|_\omega$ for an arbitrary vector $\mathbf{g} = \sum_j \langle \mathbf{g}, \psi_j^\omega \rangle_\omega \psi_j^\omega$. Recalling $Q_\omega = F_\omega^* F_\omega$ and (27), we write

$$\begin{aligned}(I - G_\omega^* G_\omega)\mathbf{g} &= (I - F_\omega^* F_\omega)\mathbf{g} + (F_\omega^* F_\omega - G_\omega^* G_\omega)\mathbf{g} \\ &= \sum_j \langle \mathbf{g}, \psi_j^\omega \rangle_\omega (1 - \mu_j^\omega)\psi_j^\omega + (F_\omega^* F_\omega - G_\omega^* G_\omega)\mathbf{g}.\end{aligned}$$

By proposition 4.3 and the orthonormality of ψ_j^ω, we have

$$\|(I - G_\omega^* G_\omega)\mathbf{g}\|_\omega \leqslant \left(\sum_j |\langle \mathbf{g}, \psi_j^\omega \rangle_\omega|^2 (1 - \mu_j^\omega)^2 \right)^{1/2} + \epsilon C_\omega \|\mathbf{g}\|_\omega. \tag{A.2}$$

Since $\mathbf{f} - \mathbf{d} = (\mathbf{f}_{\text{decay}} - \mathbf{d}) + \mathbf{f}_{\text{head}} + \mathbf{f}_{\text{tail}}$, we use (A.2) to estimate each of the three terms separately.

For the first term, we start with

$$\begin{aligned}\langle \mathbf{f}_{\text{decay}} - \mathbf{d}, \psi_j^\omega \rangle_\omega &= \langle \mathbf{f}, \psi_j^\omega \rangle_\omega - \frac{1}{\mu_j^\omega} \langle \mathbf{f}^\sharp, \psi_j^{\sharp,\omega} \rangle_\sigma \\ &= \frac{1}{\mu_j^\omega} \langle \mathbf{f}, F_\omega^* F_\omega \psi_j^\omega \rangle_\omega - \frac{1}{\mu_j^\omega} \langle \mathbf{f}, G_\omega^* G_\omega \psi_j^\omega \rangle_\omega \\ &= \frac{1}{\mu_j^\omega} \langle \mathbf{f}, (F_\omega^* F_\omega - G_\omega^* G_\omega)\psi_j^\omega \rangle_\omega,\end{aligned} \tag{A.3}$$

where $j \in J_{\text{decay}}$ and we used (27).

Note that, for any vector $\mathbf{f}$, the Cauchy–Schwarz inequality, proposition 4.3 and the orthonormality of ψ_j^ω imply the estimate

$$|\langle \mathbf{f}, (F_\omega^* F_\omega - G_\omega^* G_\omega)\psi_j^\omega \rangle_\omega| \leqslant \epsilon C_\omega \|\mathbf{f}\|_\omega. \tag{A.4}$$

Using (A.4) for (A.3) yields

$$\left|\left\langle \mathbf{f}_{\text{decay}} - \mathbf{d}, \psi_j^{\omega} \right\rangle_{\omega}\right| \leqslant \frac{\epsilon C_{\omega} \|\mathbf{f}\|_{\omega}}{\mu_j^{\omega}},$$

and thus, using our definition of C_{μ},

$$\left(\sum_{j \in J_{\text{decay}}} \left|\left\langle \mathbf{f}_{\text{decay}} - \mathbf{d}, \psi_j^{\omega} \right\rangle_{\omega}\right|^2 \left(1 - \mu_j^{\omega}\right)^2 \right)^{1/2} \leqslant \epsilon C_{\omega} C_{\mu} \|\mathbf{f}\|_{\omega}.$$

In order to bound the second term on the right-hand side of (A.2), we again use (A.3) and (A.4) to obtain

$$\|\mathbf{f}_{\text{decay}} - \mathbf{d}\|_{\omega} = \left(\sum_{j \in J_{\text{decay}}} \left(\frac{1}{\mu_j^{\omega}}\right)^2 \left|\left\langle \mathbf{f}, (F_{\omega}^* F_{\omega} - G_{\omega}^* G_{\omega}) \psi_j^{\omega} \right\rangle_{\omega}\right|^2 \right)^{1/2} \leqslant \epsilon C_{\omega} \tilde{C}_{\mu} \|\mathbf{f}\|_{\omega}.$$

Thus, in the decay region, estimate (A.2) implies

$$\|(I - G_{\omega}^* G_{\omega})(\mathbf{f}_{\text{decay}} - \mathbf{d})\|_{\omega} \leqslant (\epsilon C_{\omega} C_{\mu} + \epsilon^2 C_{\omega}^2 \tilde{C}_{\mu}) \|\mathbf{f}\|_{\omega}.$$

For $\mathbf{f}_{\text{head}}$, since $1 - \mu_j^{\omega} < \delta$, the first term in estimate (A.2) can be bounded by

$$\left(\sum_j |\langle \mathbf{f}_{\text{head}}, \psi_j^{\omega} \rangle_{\omega}|^2 (1 - \mu_j^{\omega})^2 \right)^{1/2} \leqslant \delta \|\mathbf{f}\|_{\omega},$$

and thus

$$\|(I - G_{\omega}^* G_{\omega}) \mathbf{f}_{\text{head}}\|_{\omega} \leqslant (\delta + \epsilon C_{\omega}) \|\mathbf{f}\|_{\omega}.$$

For $\mathbf{f}_{\text{tail}}$, the estimate (A.2) yields

$$\begin{aligned} \|(I - G_{\omega}^* G_{\omega}) \mathbf{f}_{\text{tail}}\|_{\omega} &\leqslant \left(\sum_{j \in J_{\text{tail}}} \left|\left\langle \mathbf{f}, \psi_j^{\omega} \right\rangle_{\omega}\right|^2 \left(1 - \mu_j^{\omega}\right)^2 \right)^{1/2} + C_{\omega} \epsilon \|\mathbf{f}\|_{\omega} \\ &\leqslant (\delta + \epsilon C_{\omega}) \|\mathbf{f}\|_{\omega}, \end{aligned}$$

where we used our assumption (57).

References

[1] Abramowitz M and Stegun I A 1970 *Handbook of Mathematical Functions* 9th edn (New York: Dover)

[2] Alpert B, Francis M and Wittmann R 1998 Near-field antenna measurements using nonideal measurement locations *IEEE Trans. Antennas Propag.* **46** 716–22

[3] Averbuch A, Coifman R, Donoho D, Elad M and Israeli M 2006 Fast and accurate Polar Fourier transform *Appl. Comput. Harmon. Anal.* **21** 145–67

[4] Averbuch A, Coifman R R, Donoho D L, Israeli M and Shkolnisky Y 2007 Framework for discrete integral transformations: I. The pseudo-polar Fourier transform *SIAM J. Sci. Comput.* to appear

[5] Beylkin G 1983 The fundamental identity for iterated spherical means and the inversion formula for diffraction tomography and inverse scattering *J. Math. Phys.* **24** 1399–400

[6] Beylkin G 1983 Iterated spherical means in linearized inverse problems *Conf. on Inverse Scattering: Theory and Application (Tulsa, OK, 1983)* (Philadelphia, PA: SIAM) pp 112–7

[7] Beylkin G 1995 On the fast Fourier transform of functions with singularities *Appl. Comput. Harmon. Anal.* **2** 363–81

[8] Beylkin G and Monzón L 2002 On generalized Gaussian quadratures for exponentials and their applications *Appl. Comput. Harmon. Anal.* **12** 332–73

[9] Beylkin G and Sandberg K 2005 Wave propagation using bases for bandlimited functions *Wave Motion* **41** 263–91 (University of Colorado, APPM preprint 518, Dec. 2003)

[10] Burridge R and Beylkin G 1988 On double integrals over spheres *Inverse Problems* **4** 1–10
[11] Candès E, Demanet L, Donoho D and Ying L 2006 Fast discrete curvelet transforms *Multiscale Model. Simul.* **5** 861–99 (electronic)
[12] Dahlquist G and Björck A 1974 *Numerical Methods* (Englewood Cliffs, NJ: Prentice-Hall)
[13] Devaney A 1982 A filtered backpropagation algorithm for diffraction tomography *Ultrason. Imaging* **4** 336–50
[14] Dutt A and Rokhlin V 1993 Fast Fourier transforms for nonequispaced data *SIAM J. Sci. Comput.* **14** 1368–93
[15] Fenn M, Kunis S and Potts D 2007 On the computation of the polar FFT *Appl. Comput. Harmon. Anal.* **22** 257–63
[16] John F 1955 *Plane Waves and Iterated Spherical Means* (New York: Interscience)
[17] Landau H J and Pollak H O 1961 Prolate spheroidal wave functions, Fourier analysis and uncertainty: II *Bell Syst. Tech. J.* **40** 65–84
[18] Landau H J and Pollak H O 1962 Prolate spheroidal wave functions, Fourier analysis and uncertainty: III *Bell Syst. Tech. J.* **41** 1295–336
[19] Lee J-Y and Greengard L 2005 The type 3 nonuniform FFT and its applications *J. Comput. Phys.* **206** 1–5
[20] Potts D, Steidl G and Tasche M 2001 Fast Fourier transforms for nonequispaced data: a tutorial *Modern Sampling Theory Appl. Numer. Harmon. Anal.* (Boston, MA: Birkhäuser) pp 247–70
[21] Press W H and Rybicki G B 1989 Fast algorithm for spectral analysis of unevenly sampled data *Astrophys. J.* **338** 227–80
[22] Shkolnisky Y 2007 Prolate spheroidal wave functions on a disc—integration and approximation of two-dimensional bandlimited functions *Appl. Comput. Harmon. Anal.* **22** 235–56
[23] Slepian D 1964 Prolate spheroidal wave functions, Fourier analysis and uncertainty: IV. Extensions to many dimensions; generalized prolate spheroidal functions *Bell Syst. Tech. J.* **43** 3009–57
[24] Slepian D 1965 Some asymptotic expansions for prolate spheroidal wave functions *J. Math. Phys.* **44** 99–140
[25] Slepian D 1978 Prolate spheroidal wave functions, Fourier analysis and uncertainty: V. The discrete case *Bell Syst. Tech. J.* **57** 1371–430
[26] Slepian D and Pollak H O 1961 Prolate spheroidal wave functions, Fourier analysis and uncertainty: I *Bell Syst. Tech. J.* **40** 43–63
[27] Xiao H, Rokhlin V and Yarvin N 2001 Prolate spheroidal wavefunctions, quadrature and interpolation *Inverse Problems* **17** 805–38